Scientific Reports

https://doi.org/10.1038/s41598-026-39416-4

Article in Press

Loss of mechanical stress induces synovitis, fibrosis and articular cartilage degeneration via distinct synovial cell subsets

Received: 1 December 2025

Accepted: 4 February 2026

Published online: 09 February 2026

Cite this article as: Ishikura H., Okada H., Kin Y. *et al.* Loss of mechanical stress induces synovitis, fibrosis and articular cartilage degeneration via distinct synovial cell subsets. *Sci Rep* (2026). https://doi.org/10.1038/s41598-026-39416-4

Hisatoshi Ishikura, Hiroyuki Okada, Yota Kin, Ryota Chijimatsu, Junya Higuchi, Junya Miyahara, Naohiro Tachibana, Kosei Nagata, Asuka Terashima, Fumiko Yano, Yasunori Omata, Masahide Seki, Yutaka Suzuki, Roland Baron, Sakae Tanaka & Taku Saito

Loss of mechanical stress induces synovitis, fibrosis and articular cartilage degeneration via distinct synovial cell subsets

Hisatoshi Ishikura[1], Hiroyuki Okada[3], Yota Kin[1], Ryota Chijimatsu[2], Junya Higuchi[1], Junya Miyahara[1], Naohiro Tachibana[1], Kosei Nagata[1], Asuka Terashima[2], Fumiko Yano[2], Yasunori Omata[2], Masahide Seki[4], Yutaka Suzuki[4], Roland Baron[5], Sakae Tanaka[1], and Taku Saito[1]*

[1]Sensory and Motor System Medicine, Graduate School of Medicine, The University of Tokyo, 7-3-1 Hongo, Bunkyo-ku, Tokyo 113-8655, Japan.

[2]Bone and Cartilage Regenerative Medicine, Graduate School of Medicine, The University of Tokyo, 7-3-1 Hongo, Bunkyo-ku, Tokyo 113-8655, Japan.

[3]Center for Disease Biology and Integrative Medicine, Graduate School of Medicine, The University of Tokyo, 7-3-1 Hongo, Bunkyo-ku, Tokyo 113-8655, Japan.

[4]Laboratory of Systems Genomics, Department of Computational Biology and Medical Sciences, The University of Tokyo, 5-1-5 Kashiwanoha, Kashiwa City, Chiba, Japan.

[5]Department of Medicine, Harvard Medical School, Endocrine Unit,

MGH, and Harvard School of Dental Medicine, 188 Longwood Ave, Boston, MA, USA.

*Correspondence should be addressed to:

Associate Professor Taku Saito, MD, PhD

Sensory and Motor System Medicine, Graduate School of Medicine, The University of Tokyo, Hongo 7-3-1, Bunkyo-ku, Tokyo 113-8655, Japan.

Tel: (+81)-3-3815-5411 (ext. 37369); Fax: (+81)-3-3818-4082

E-mail: tasaitou-tky@umin.ac.jp

The authors have declared that no conflict of interest exists.

Abstract

Joint function is impaired by disuse, as well as overuse. However, the underlying mechanisms remain unclear. Here, we elucidate the mechanisms of synovial and cartilage changes using a minimized mechanical stress (MMS) mouse model by combining knee joint immobilization and unloading. In this model, synovitis appeared by day 3, followed by subsequent fibrosis leading to joint contracture within two weeks. In contrast, articular cartilage degeneration developed gradually after the synovial alterations. Notably, synovial changes were attenuated by discontinuation of joint immobilization, while cartilage changes improved after discontinuation of joint immobilization and loading. Bulk RNA sequencing (RNA-seq) analyses supported the transcriptomic alterations for synovitis, fibrosis, and cartilage degeneration, and identified ten cytokines associated with cartilage changes. Single-cell RNA-seq (scRNA-seq) further identified distinct subsets in the MMS synovium: *Lrrc15*$^{+}$ myofibroblasts and *Mmp9*$^{+}$ macrophages, expressing many of these cytokines. Histological examination showed that MMS initially induced macrophage proliferation, while macrophage depletion by intra-articular administration of clodronate liposomes inhibited MMS-induced synovitis, fibrosis and cartilage degeneration, accompanied by a marked reduction in the MMS-distinct subsets. Our findings identified MMS-induced alterations in synovial cells and

their roles in joint phenotype, suggesting that joint motion and mechanical loading contribute to the regulation of joint homeostasis.

Introduction

Cartilage and the surrounding synovium are fundamental components of articular joints. The synovium consists of various types of fibroblasts, macrophages, and other immune cells. Synovitis, triggered by these immune cells, is associated with joint diseases such as rheumatoid arthritis (RA) and osteoarthritis (OA), the most prevalent joint disorder worldwide. In knee OA, the severity of joint pain is closely linked to the presence of synovitis[1]. Given that synovitis is significantly associated with subsequent OA progression[2], the synovium likely plays an essential role in cartilage maintenance in healthy joints, although the mechanisms of synovium–cartilage interaction remain poorly understood.

Various factors, such as aging, obesity, joint instability, trauma, and overuse, are associated with OA pathogenesis[3, 4]. Excessive mechanical loading on cartilage is considered a common underlying factor for these pathogenic factors[5]. In addition, disuse adversely affects joint function, leading to contracture and atrophy of cartilage and bone, as observed in conditions resulting from paralysis due to brain infarction or spinal cord injury, or immobilization during fractures[6-8]. This indicates that the absence of mechanical forces, known to cause bone loss[9], is also detrimental to articular joints. Interestingly, joint motion exercise can alleviate OA symptoms, including joint pain[10-12]. Although appropriate use

maintains the homeostasis of synovial joints, the underlying mechanisms remain unidentified.

To investigate the effects of joint motion and loading on the synovium and cartilage, we established a mouse model of immobility and unloading through tail suspension and knee joint immobilization. We then explored synovium–cartilage interactions and the alterations caused by the loss of mechanical stress on joints. Comprehensive analysis using RNA sequencing (RNA-seq) and single-cell technology provided novel insights into how the loss of mechanical stress affects cellular interactions between the synovium and cartilage and leads to synovitis and cartilage degeneration.

Results

Synovitis and fibrosis precede cartilage degeneration by joint immobilization and unloading.

To investigate the role of mobility and loading in joint integrity, we developed a minimized mechanical stress (MMS) model by combining knee joint immobilization with a plastic cylinder and unloading via tail suspension (Fig. 1a-c). The range of passive knee joint motion was significantly reduced at 2 weeks in the MMS model (Supplementary Fig. 1a, b). Micro-computed tomography (μCT) revealed a thinner femoral cortex and reduced trabeculae in the femoral head, with bone morphometric parameters indicating MMS-

induced bone fragility (Supplementary Fig. 1c, d).

Histological examination showed progressive thickening of the synovial lining layer in MMS joints, accompanied by neovascularization and perivascular accumulation of inflammatory cells (Fig. 1d, e, Supplementary Fig. 2). Masson's trichrome staining further demonstrated fibrosis in the sublining area (Supplementary Fig. 2). These alterations were most obvious at 2 weeks (Fig. 1d, e) and preceded cartilage degeneration, which was observed after 2 weeks and continued to progress until 6 weeks, with surface irregularities and clefts (Fig. 1d, f). These findings indicate that the synovial response to the loss of mechanical stress occurs much earlier than cartilage degeneration.

Joint motion restores the synovial alterations, and the combination of joint motion and weight bearing attenuates cartilage degeneration.

Next, we examined the reversibility of these changes using the following re-mobilization and re-loading models: R1, where only joint motion is resumed after a 2-week period, and R2, where both joint motion and weight bearing are restored at 2 weeks (Fig. 1c). Compared to the MMS mice at day (D) 14 or 28, synovitis significantly improved in both R1 and R2 mice (Fig. 1d, e). Cartilage degeneration was also reversed in both models, but more notably in the R2 model (Fig. 1d, f). These results demonstrate that the

synovium is regulated by joint motion, while the cartilage is regulated by both joint motion and weight bearing.

Immobilization, not unloading, leads synovium to express genes related to fibrosis and cartilage degradation.

Next, we investigated changes in the synovium transcriptome using bulk RNA-seq at each time point. The expression patterns underwent sequential alterations throughout the time course of the MMS model and were subsequently reversed in the R1 and R2 models, returning to levels comparable to those observed in the control group (Fig. 2a, b). These alterations in gene expression in synovium aligned with the histological changes observed in synovium (Fig. 1d, e). Genes were categorized into five modules according to their expression patterns, and their characteristic Gene Ontology (GO) terms were extracted (Fig. 2a, c). GO analysis indicated that genes in groups C and E, which encompassed terms associated with the extracellular matrix, were gradually upregulated in the MMS model and downregulated in the R1 and R2 models (Fig. 2a, c). In contrast, expression of genes in module A, which included terms related to the negative regulation of fibroblasts and macrophages, was markedly downregulated in the MMS model, particularly at D7 and 14 (Fig. 2a, c). We then examined differentially expressed genes among extracellular matrix or collagen-related genes. The expression of fibrosis-related genes such as *Spp1*, *Col1a1, Ibsp, Col1a2,* and *Postn* that was upregulated

from D7 to 14 in the MMS synovium (Fig. 2d). Similarly, the expression of cartilage degradation-related enzymes such as *Mmp13* and *Mmp9* increased after D7 in the MMS synovium (Fig. 2d). These gene expression changes were reversed in the R1 and R2 models (Fig. 2d). These data suggest that joint motion contributes to attenuating the activation of synovial fibroblasts and macrophages, thereby preventing synovial fibrosis and the secretion of factors that promote articular cartilage degradation.

The combination of unloading and immobilization remarkably decreases anabolic genes in cartilage.

We conducted analyses on cartilage samples throughout the duration of the MMS model, similar to those performed on the synovium mentioned above. The transcriptome profiles revealed that the expression patterns altered sequentially throughout the progression of the MMS model (Fig. 3a, b). These patterns partially approached control levels when joint immobilization was discontinued (R1) and nearly returned to control levels when both unloading and immobilization were removed (R2) (Fig. 3b). These alterations in gene expression in cartilage aligned with the histological changes observed in articular cartilage (Fig. 1d, f). Genes were categorized into five modules according to their expression patterns, and their characteristic GO terms were extracted (Fig. 3a, c). Various terms related to cartilage and chondrocytes in module E decreased from

D7 to 28, and most of these changes were reversed in the R2 model (Fig. 3c). We then examined differentially expressed genes among cartilage- or tissue remodeling-related genes. Cartilage matrix genes such as *Col2a1*, *Col11a1*, *Col11a2*, *Acan*, and *Prg4*, along with essential transcription factors for chondrocyte differentiation and cartilage matrix gene induction such as *Sox9* and *Sox5*, decreased due to MMS after D7 (Fig. 3d). In the R2 model, the expression levels of these genes, except for *Prg4*, returned to levels comparable to those observed in the control group, whereas in the R1 model, they only partially reverted toward control levels (Fig. 3d). The difference observed between R1 and R2 models suggests that both joint motion and mechanical loading are required for maintaining cartilage homeostasis through inducing the expression of chondrogenic and cartilage matrix genes.

Synovium of immobilized joints expresses molecules considered upstream regulators of cartilage degeneration.

The time-course analyses of histology and gene expression implied that alterations in the synovium might lead to cartilage degeneration in immobilized and unloaded joints. To investigate the synovium–cartilage interactions responsible for cartilage degeneration, we first examined the expression of genes encoding secreted molecules. Immune-related cytokines and chemokines, such as *Il1b*, *Il11*, *Ccl2*, *Osm*, and *Lif,* began to increase at D3 (Fig. 4a), aligning with early

histological changes in the synovium. Subsequently, cytokines related to extracellular matrix production, such as *Spp1*, *Tgfb3*, and *Tgfb1*, were upregulated (Fig. 4a). In the cartilage, fewer cytokines were detected (Fig. 4a). Interestingly, most of them were commonly upregulated in both the MMS synovium and cartilage, including the pain-related factor *Ngf*, the cartilage-protective factor *Timp1*, and the osteoclastogenesis-related *Tnfsf11* (Fig. 4a). The alterations in gene expression of these secreted molecules in both the synovium and cartilage were reversible, returning to baseline levels once joint mobility was restored (Fig. 4a).

We further performed ingenuity pathway analysis (IPA) to infer potential upstream cytokines influencing cartilage gene expression changes in the MMS model at D14 (Fig. 4b). Among the 46 candidates predicted by IPA, 10 genes were upregulated in the MMS synovium (Fig. 4a-c), including *Tgfb*, *Il1b, Osm*, *Tnfsf11*, *Spp1*, *Lif, Il11*, and *Ccl2*. Only one gene (*Tnfsf11)* was upregulated in both the MMS synovium and cartilage (Fig. 4a-c). In contrast, there were no cartilage-specific genes among the 10 candidate genes (Fig. 4c). These findings are consistent with the notion that synovial-derived signals may be associated with cartilage gene expression changes in immobilized joints, potentially through paracrine interactions.

Distinct fibroblast and macrophage subsets emerge in the MMS synovium.

Next, we performed single-cell RNA sequencing (scRNA-seq) analysis using synovium-derived cells from control and MMS D14 samples. Synovial tissues were collected from both knees of 10 control mice (20 knees) and 10 MMS D14 mice (20 knees). Tissues from each group were pooled prior to cell isolation and processed as a single scRNA-seq library per group. A total of 7,898 cells were categorized into 16 clusters based on their marker gene expression profiles: 9 fibroblast clusters, 4 macrophage clusters, and one each for endothelial cells, smooth muscle cells, and lymphocytes (Fig. 5a, b). Among fibroblast clusters, universal clusters highly expressing *Pi16*, *Dpp4*, *Penk*, and *Col15a1*, as identified by Buechler *et al*[13], were predominant in the control synovium (clusters 2, 3, 6, 13) (Fig. 5a-c). The number of *Pi16*$^{+}$*Dpp4*$^{+}$ and *Penk*$^{+}$ fibroblasts (clusters 2, 3) was markedly decreased in the MMS model (Fig. 5c). Lining fibroblasts expressing *Prg4* (cluster 1) were more abundant in the MMS model, corresponding with thickening of the lining layer (Fig. 1d, 5c). Notably, the *Lrrc15*$^{+}$ subset (cluster 9), characterized as myofibroblasts, was distinct in the MMS synovium (Fig. 5a-c). The *Lrrc15*$^{+}$ fibroblasts strongly expressed multiple fibrosis-related genes, including *Cdh11*, *Col1a1*, *Postn*, *Spp1*, and *Sparc* (Fig. 5c).

Cells in the macrophage clusters were divided into four subsets, clusters 4, 7, 8, and 10 (Fig. 5a, b). The *Cx3cr1*$^{+}$ subset (cluster 4) was characterized as tissue-resident lining macrophages, while the major histocompatibility complex class II (MHCII)$^{+}$ subset

(cluster 8) was characterized as proliferating interstitial macrophages[14] (Fig. 5a, b). In contrast to other macrophages (clusters 4, 7, and 8), cells in cluster 10 expressed *Mmp9*, *S100a9*, *Cxcl2*, *Il1b*, and *Osm* (Fig. 5b). The *Mmp9*$^{+}$ macrophage subset was distinct in the MMS model, as well as the *Lrrc15*$^{+}$ fibroblasts (Fig. 5c).

Estimation of synovial cell subsets associated with MMS.

To examine subsets associated with the MMS-induced synovitis, we analyzed GO terms related to “inflammation” or “inflammatory” (Fig. 6a). As expected, the four macrophage subsets (clusters 4, 7, 8, and 10) were predominantly represented in these terms (Fig. 6a). Terms such as “leukocyte migration involved in inflammatory response,” “chronic inflammatory response,” “positive regulation of cytokine production involved in inflammatory response,” and “inflammatory cell apoptotic process” were specifically upregulated in the *Mmp9*$^{+}$ macrophages (Fig. 6a). Furthermore, in the *Mmp9*$^{+}$ macrophages, terms such as “negative regulation of acute inflammatory response to antigenic stimulus,” “negative regulation of chronic inflammatory response,” and “negative regulation of inflammatory response to antigenic stimulus” were downregulated compared to other macrophage subsets (Fig. 6a). Next, we analyzed GO terms related to “mechano” or “mechanical” (Fig. 6b). GO terms including “mechanical” were upregulated in sublining fibroblast clusters 2, 3,

5, 6, and 9, but not in *Prg4*$^{+}$ lining fibroblasts, macrophages, and lymphocytes (Fig. 6b). Among these fibroblasts, “detection of mechanical stimulus” and “response to mechanical stimulus” were the most prominent in the *Lrrc15*$^{+}$ myofibroblasts (Fig. 6b). These findings suggest that macrophages, particularly the *Mmp9*$^{+}$ macrophage subset, may be involved in MMS-induced synovitis, while certain fibroblasts might be responsible for sensing motion and mechanical loading on the joint.

We further analyzed the cellular origin of the ten synovium-derived cytokines potentially contributing to cartilage changes. *Tgfb3*, *Spp1*, and *Pdgfc* were mainly expressed in the *Lrrc15*$^{+}$ myofibroblasts, while *Il1b* and *Osm* were predominantly expressed in the *Mmp9*$^{+}$ macrophages (Fig. 6c, d). The *Lrrc15*$^{+}$ myofibroblasts also expressed *Tnfsf11* and *Il11* (Fig. 6c, d). *Tgfb1* was expressed in various macrophages and fibroblasts (Fig. 6c, d). These data suggest that MMS-specific fibroblasts and macrophages may also play key roles in MMS-induced cartilage changes.

Macrophages show an early response to MMS and are responsible for MMS-induced alterations in the synovium and cartilage.

We next investigated the time-course distribution of fibroblasts and macrophages in the MMS synovium (Fig. 7a). Immunohistochemical analysis revealed an initial increase in CD68^{+} macrophages in the

lining layer on D3, followed by their expansion into the sublining area (Fig. 7a, b). In contrast, a significant increase in fibroblasts, determined by COL1A1 expression, was observed on D7 (Fig. 7a, b).

To examine the pathogenic role of macrophages in the MMS model, we depleted synovial macrophages by intra-articular administration of clodronate liposomes (CLNs) every two weeks (Fig. 7c). Quantitative analysis of CD68 immunostaining demonstrated effective macrophage depletion by clodronate treatment. Compared with MMS D14, CD68-positive cells were reduced by 84% in the synovial lining layer and by 66% in the sublining region in the CLN+MMS D14 group (Fig. 7b). In the CLN injection group, fibroblast proliferation and the subsequent synovial fibrosis were significantly reduced by D14 (Fig. 7a, b).

Furthermore, MMS-induced cartilage degeneration was significantly attenuated in the CLN injection group at both D28 and 42 (Fig. 7d, e). The marker genes for *Lrrc15*$^{+}$ myofibroblasts were upregulated in the MMS synovium; however, CLN treatment markedly suppressed their expression, as well as that of *Mmp9* (Fig. 7f). Collectively, these findings suggest that macrophages play a key role in activating fibroblasts and promoting subsequent cartilage degradation in response to MMS.

Discussion

Our study demonstrated that the disruption of joint homeostasis occurred following the removal of mechanical stress from joints, through tail suspension and joint immobilization (MMS). Inflammation and fibrosis progressively developed in the synovium under MMS conditions, leading to cartilage degeneration. These histological changes were partially reversible, with the observed transitions and reversibility corresponding to time-course alterations in gene expression profiles of the synovium and cartilage, as revealed by RNA-seq analysis. In the synovium, the expression of extracellular matrix, fibrosis-, and immune-related genes showed increased expression in the MMS model. In the cartilage, the expression of extracellular matrix and chondrogenic genes progressively declined in the MMS model. Ten genes, identified as potential upstream secreted molecules responsible for cartilage changes, were upregulated in the MMS synovium. Among the fibroblast and immune cell subsets determined by scRNA-seq, *Lrrc15*$^{+}$ myofibroblasts and *Mmp9*$^{+}$ macrophages were distinct in the MMS model compared to the control. The ten candidate cytokine genes potentially responsible for MMS-induced cartilage changes were predominantly expressed in these MMS-distinct clusters. Histological analysis indicated that macrophage proliferation preceded fibroblast activation. Macrophage depletion via intra-articular administration of CLN prevented fibroblast proliferation, synovial fibrosis, and subsequent cartilage degeneration. These

findings imply that the loss of joint motion and/or mechanical loading in the MMS model impair joint homeostasis through complex mechanisms, highlighting the necessity of appropriate joint motion and/or mechanical loading for maintaining normal synovium and cartilage.

Macrophages appear to play a major role in the synovitis and cartilage degeneration caused by MMS, based on the observations that 1) macrophage proliferation was initially observed in response to MMS, and 2) macrophage depletion inhibited the MMS-induced changes (Fig. 7a-e). The *Mmp9*$^{+}$ macrophages in the MMS synovium exhibited strong proinflammatory features. *Cxcl2*, *Il1b*, *Osm*, and *S100a9*, which are characteristic of *Mmp9*$^{+}$ macrophages (Fig. 5b), are also highly expressed in inflammatory macrophages under other pathological conditions, such as Crohn's disease and atherosclerosis[15, 16]. In synovial macrophages of patients with RA, S100A9 expression is positively correlated with disease activity[17]. In human OA, inflammatory macrophages and monocytes express high levels of IL1B[18, 19]. In addition to these cytokines and chemokines, MMP9 is a well-known catabolic enzyme associated with the activity or severity of OA[20-22]. MMP9 is a target gene of nuclear factor kappa B (NF-κB)[23], a key transcription factor involved in the pathogenesis of OA[24]. In addition, MMP9 activates various cellular processes through proteolytic shedding, including transforming growth factor (TGF)-β[25], a potent fibroblast activator crucial for the conversion of

fibroblasts to myofibroblasts[26]. IL-1β and MMP9 also promote myofibroblast activation through upregulation of TGF-β[27,28]. Thus, the molecules expressed in the *Mmp9*$^{+}$ macrophages are likely involved in the activation and proliferation of myofibroblasts.

The immobility and unloading significantly decreased the number of universal fibroblasts and increased the number of *Lrrc15*$^{+}$ myofibroblasts in the synovium (Fig. 5c). A recent cross-tissue fibroblast atlas identified universal pan-tissue *Pi16*$^{+}$ and *Col15a1*$^{+}$ fibroblast subsets in healthy mice, while *Lrrc15*$^{+}$ myofibroblasts were specifically detected in pathological conditions such as arthritic joints, fibrotic organs, and wounds in mice[13]. Based on the current gene expression data of various fibrosis-related genes, including *Col1a1*, *Spp1*, *Cdh11*, *Tgfb3*, *Fmod*, and *Sparc* (Fig. 5b), the *Lrrc15*$^{+}$ myofibroblast cluster appears to be a key cell subset contributing to synovial fibrosis in MMS joints.

Mechanical stress-related GO terms were markedly enriched in five sublining fibroblast clusters: *Pi16*$^{+}$*Dpp4*$^{+}$, *Penk*$^{+}$, *Fap*$^{+}$, and *Col15a1*$^{+}$ fibroblasts (clusters 2, 3, 5, 6) and *Lrrc15*$^{+}$ myofibroblasts (cluster 9) (Fig. 6b). These GO terms were also detected in other fibroblasts (clusters 12–14), endothelial cells (cluster 0), and vascular smooth muscle cells (cluster 11). In contrast, they were downregulated in all macrophage clusters (clusters 4, 7, 8, 10) and lymphocytes (cluster 15) (Fig. 6b). Histological analysis further demonstrated that macrophage proliferation preceded fibroblast

activation (Fig. 7a, b). These findings suggest that mechanical stress on the synovium may initially be sensed by synovial fibroblasts and vascular cells, which subsequently stimulate macrophages, ultimately leading to the induction of the *Lrrc15*$^{+}$ myofibroblasts. At present, there are no reports indicating that synovial macrophages are altered by joint disuse; however, mechanosensitivity of macrophages has been reported in primary culture and in several non-articular tissues, such as the lung, liver, and central nervous system[29,30]. Although the mechanosensing system of synovial cells could not be experimentally determined in the present study, the reciprocal interactions between fibroblasts and macrophages appear to accelerate synovitis, fibrosis, and cartilage degeneration under the MMS condition.

Both joint motion and mechanical loading are required for articular cartilage homeostasis (Fig. 1d, f). Joint motion influences articular cartilage through two mechanisms: direct effects of mechanical stress on the articular cartilage itself and indirect effects mediated by the synovium. Regarding direct effects, previous studies reported that mechanical loading enhances the production of extracellular matrix[31]. Consistent with this, expression levels of various cartilage matrix genes, such as *Prg4*, are decreased by MMS (Fig. 3d). Lubricin, an essential extracellular matrix protein encoded by the proteoglycan 4 (*Prg4*) gene, is produced by chondrocytes in the superficial articular cartilage and by fibroblasts in the synovial

lining layer. Its loss of function leads to juvenile idiopathic arthritis in both humans and mice[32, 33]. Interestingly, lubricin is induced by shear stress on the articular cartilage surface[34]. We previously reported that lubricin contributes to joint homeostasis by modulating the differentiation of superficial zone cells as a signaling molecule and inhibiting the NF-κB-MMP9-TGF-β pathway[36]. Regarding indirect effects mediated by the synovium, ten secreted molecules upregulated in the MMS synovium are potential upstream regulators of cartilage degeneration (Fig. 4c). Among these, receptor activator of nuclear factor kappa B ligand (RANKL), encoded by *Tnfsf11*, is required for osteoclastogenesis and regulates bone resorption in RA and subchondral bone remodeling in OA[36-38]. TGF-β1, which regulates fibrosis, osteophyte formation, and subchondral bone remodeling[39-41], was widely expressed in immune cells and myofibroblasts (Fig. 5b). Osteopontin (*Spp1*), a fibrosis-related factor in various organs[43], was specifically expressed in myofibroblasts (Fig. 5b). Interleukin (IL)-1β, CCL2, and oncostatin M (OSM) are representative proinflammatory cytokines associated with RA and OA pathogenesis[18, 44, 45]. *Il1b* and *Osm* were predominantly expressed in *Mmp9*$^{+}$ macrophages, while *Ccl2* was expressed in other macrophages (Fig. 6c, d). These results suggest that *Lrrc15*$^{+}$ myofibroblast and *Mmp9*$^{+}$ macrophage subsets play major roles in cartilage changes caused by MMS.

This study has several limitations that should be

acknowledged. First, in the present model, immobilization and unloading cannot be completely separated. Although our re-mobilization paradigms (R1 and R2) provide insight into the differential contributions of joint motion and mechanical loading, dedicated groups involving immobilization alone or unloading alone would be required to fully disentangle these effects. Second, although integrated transcriptomic analyses and IPA offer valuable insights into potential signaling pathways linking synovial inflammation and cartilage degeneration, the identified upstream regulators should be interpreted as bioinformatically inferred candidates rather than definitive causal drivers. Accordingly, the proposed synovium–cartilage signaling axis represents a working hypothesis that requires targeted functional validation in future studies. Third, while our time-course analysis suggests that synovial macrophage expansion precedes fibroblast activation, the temporal resolution of the current study is inherently limited by the selection of discrete observational time points, which may not fully capture the optimal timing of cellular dynamics. Therefore, the proposed sequence should be interpreted as a temporal association rather than definitive proof of causality. Fourth, because the scRNA-seq experiments were performed using pooled samples per condition, differences in cell cluster proportions and gene expression patterns should be interpreted as exploratory. Independent biological replication will be required in future studies to statistically validate

these findings. Finally, although macrophage depletion was substantial, it was incomplete, and pharmacological depletion approaches inherently lack absolute cellular specificity. These limitations should be considered when interpreting the functional contribution of synovial macrophages to joint pathology.

Overall, our study reveals the changes and roles of synovial immune cells in joints subjected to immobilization and unloading, highlighting the crucial impact of mechanical stress on joint homeostasis. Further insights into the synovial macrophage-fibroblast axis may lead to the development of disease-modifying therapeutics for joint disorders.

Methods

Mice

C57BL/6J wild-type male mice were purchased from Sankyo Labo Service Corporation (Tokyo, Japan). Among them, mice aged 8 to 14 weeks were used as controls. Both control and MMS model mice were housed in plastic cages with ALPHA-dri bedding (Shepherd Specialty Papers) in a specific pathogen-free facility. The room had a 12-h light/dark cycle and was maintained at a constant temperature (18–22℃). All mice were euthanized by CO_2 inhalation at the time of sacrifice. For this experiment, no inclusion or exclusion criteria were set.

MMS model

MMS model mice were suspended by their tails at 8 weeks of age. First, adhesive tape was applied to their tails. Their knee joints were then kept immobilized using plastic cylinders[46]. Their feet were also taped to prevent the plastic cylinders from sliding off. Additional adhesive tape was applied between the rear limbs so that the mice could not bite the tape around their tail. Following joint fixation, their tails were suspended by attaching a spring clip to the adhesive tape. The spring clip was connected to piano wire attached to the cage lid, allowing the mice to move within their cages. Food was left on the floor, and a water bottle was fixed to the wall with double-sided tape for easy access.

The time points used in this study were selected based on preliminary experiments indicating that synovial inflammatory responses begin to emerge within the first 1–2 weeks after joint immobilization, whereas fibrotic remodeling and cartilage degeneration develop more gradually over several weeks. To capture the early initiation of synovial inflammation, we included an additional early intermediate time point at day 3, which allowed assessment of initial transcriptional and histological changes preceding overt tissue remodeling. Accordingly, early (D3–D14) and later (4–6 weeks) time points were chosen to capture both the initiation and progression phases of MMS-induced joint pathology,

while balancing animal numbers and experimental complexity.

Measurement of the range of motion of the knee joint

Mice were anesthetized with isoflurane, induced at a concentration of 4–5% and maintained at 2–3%, and a push/pull tension gauge (Teclock) was attached to their foot. The range of motion of the knee joint was measured using a push/pull force of 0.05 N.

μCT

μCT images were obtained using an inspeXio SMX-100CT (Shimadzu Corporation). The proximal part of the femur was used to assess bone structure. The imaging conditions were as follows: voltage, 75 kV; current, 140 μA; voxel size, 0.012 mm/voxel; image size, 512 × 512 pixels; and slice thickness, 0.02 mm. The original three-dimensional images were displayed, and the following parameters were calculated using bone microstructure software (TRI/3D-BON-FCS64, RATOC System Engineering): the ratio of bone volume to total callus volume (BV/TV), the star volume of the bone marrow space (V*m space), and the structure model index[47]. These parameters were evaluated at the femoral head without involving the epiphyseal line under specified conditions.

Histological analyses and immunostaining

Tissue samples were fixed with 4% paraformaldehyde in phosphate-

buffered saline (pH 7.4) and then delipidated with 100% methanol at room temperature. Specimens were decalcified with 10% ethylenediaminetetraacetic acid (pH 7.4) at 4℃ for 4 to 5 days with stirring and then embedded in paraffin. The knee joints were sectioned sagittally, and 5-μm-thick sections were prepared for histological evaluation. Synovial pathology was evaluated in the intercondylar area, whereas cartilage degeneration was assessed in the medial compartment. These analyses were performed using samples from eight mice (n = 8 knees) per group. For each knee, three sections spaced 60 μm apart were selected for evaluation. In each section, histological scoring was performed at three randomly selected fields, and the median value of these fields was used as the representative score for that section. The final histological score for each knee was calculated as the mean of the scores obtained from the three sections. Synovial inflammation was graded using the synovitis score based on hematoxylin and eosin–stained sections[48], whereas cartilage degeneration was assessed using the Osteoarthritis Research Society International–modified Mankin score based on safranin O–stained sections[49]. Hematoxylin and eosin staining and safranin O staining were performed according to standard protocols. For Masson's trichrome staining, deparaffinized sections were mordanted with Bouin's solution (Muto Pure Chemicals) and stained with freshly prepared iron hematoxylin. After brief differentiation with a second mordant, sections were treated

with 1% acetic acid and stained sequentially with Orange G, Masson's staining solution B, phosphotungstic acid, and aniline blue (all from Muto Pure Chemicals).

For immunohistochemistry, deparaffinized sections were treated with 0.3% hydrogen peroxide in methanol to quench endogenous peroxidase activity, followed by protease-based antigen retrieval. Non-specific binding was blocked by incubation with Blocking One Histo (Nacalai Tesque) for 10 min at room temperature. Sections were then incubated with antibodies against COL1A1 (1:500; ab6308, Abcam) or CD68 (1:1,000; ab125212, Abcam) for 60 min at room temperature. After reacting with horseradish peroxidase-conjugated antibodies for 30 min at room temperature, positive signals were visualized with diaminobenzidine (DAB). Images of all slides were captured using a NanoZoomer S60 (Hamamatsu Photonics). Positive areas for DAB were quantified using Aperio ImageScope software (Leica Microsystems)[50]. Immunohistochemical analyses were performed using knee joints from five mice (n = 5 knees) per group. All histological evaluations were performed in a blinded manner.

Quantitative reverse transcription-polymerase chain reaction (qRT-PCR)

For qRT-PCR analysis, synovial tissue was collected from mouse knee joints using the same surgical procedures as described for bulk RNA-

seq. Tissues from both knees of a single mouse were pooled and treated as one biological sample. Total RNA was purified using a Direct-zol RNA MicroPrep Kit (Zymo Research). Total RNA (0.5–1 µg) was reverse transcribed using ReverTraAce qPCR RT Master Mix without gDNA Remover (Toyobo). Each polymerase chain reaction (PCR) reaction contained 1 × THUNDERBIRD SYBR qPCR Mix (Toyobo), 0.3 µM specific primers, and 20 ng of cDNA. mRNA levels of target genes were normalized to those of β-actin. Expression levels for each target gene were calculated using the ΔΔCt quantification method. All reactions were run in triplicate on a Thermal Cycler Dice instrument (Takara Bio). The primer sequences used are listed in Supplementary Table 1.

Preparation for bulk RNA-seq

For tissue collection, mice were shaved and a midline longitudinal skin incision was made over the knee joint. The joint was exposed using a medial parapatellar approach, and the patella was gently dislocated laterally. Synovial tissue within the joint cavity was carefully excised using micro forceps and micro scissors under a stereomicroscope, avoiding contamination from surrounding ligaments or adipose tissue. For cartilage collection, the femur and tibia were separated, and articular cartilage was selectively harvested from the femoral and tibial joint surfaces using a sharp scalpel. All tissue dissections were performed under microscopic

visualization to ensure precise isolation of synovial tissue and articular cartilage. For each biological replicate, tissues from both knees of a single mouse were pooled and treated as one independent sample (n = 1 mouse). For synovial tissue, bulk RNA-seq was performed using independent samples from n = 3 mice per group, whereas for articular cartilage, independent samples from n = 2 mice per group were analyzed. Each sample was processed and sequenced independently without pooling across animals. These tissues were homogenized, and total RNA was extracted using TRI Reagent (Molecular Research Center, Inc.). Subsequently, total RNA was purified using a Direct-zol RNA MicroPrep Kit (Zymo Research) and analyzed in bulk per group. RNA integrity was assessed using an Agilent Bioanalyzer 2100 (Agilent Technologies), and only samples with an RNA integrity number (RIN) ≥ 7 were used for RNA-seq analysis. RNA library preparation and sequencing were performed by BGI using their standard bulk mRNA-seq library construction protocols. Sequencing was performed with a 50-bp single-end strategy using the BGISEQ-500 platform or a 100-bp paired-end strategy using the DNBSEQ platform, yielding approximately 4.4 Gb of clean data (~44 million reads) per sample on average. Differential gene expression analysis for bulk RNA-seq was performed using the PoissonDis method as implemented by the sequencing service provider. P-values were corrected for multiple testing, and false discovery rates (FDRs) were calculated. Genes with a fold change ≥

2.0 and FDR ≤ 0.001 were defined as differentially expressed.

Bulk RNA-seq *in silico* analysis

Reads were mapped to the reference mouse genome (mm10). A web-based transcriptomic analysis platform, iDEP (version 0.91), was used to analyze differential gene expression and compare the data at different time points[51]. The application was also used to generate heatmaps, conduct principal component analyses (PCAs), and calculate values for Pearson's correlation matrix.

For the synovium, we employed a fragments per kilobase of exon per million mapped fragments (FPKM) cutoff value of > 1 and a fold change (MMS D14/control) cutoff of < 0.67 or > 1.5. As a result, 1,178 genes were included. For the cartilage, we employed an FPKM cutoff value of > 1 and a fold change (MMS D28/control) cutoff of < 0.67 or > 1.5. As a result, 1,606 genes were included.

Data visualization was performed using R 4.4.1[52] and ggplot2[53]. Heatmaps were drawn using ComplexHeatmap[54]. As shown in Fig. 2a and 3a, hierarchical clustering was performed in both the gene and sample directions. Scaling was performed in the direction of the gene. Genes were divided into five modules. PCA of gene expression was conducted using the prcomp function in stats. The correlation matrix of gene expression was constructed using the corrr package[55]. Gene sets in each module were annotated considering the composed genes in GO terms from the latest

mSigDB[56] (m5.all.v2023.2.Mm.symbols.gmt), including {“inflammation,” “mechano,” “fibroblast,” “extracellular,” “chondro,” “cartilage,” “macrophage,” “immune”}.

IPA[57] was performed to infer potential upstream cytokines associated with cartilage gene expression changes. We used cartilage data from the MMS D14. We selected 2,401 genes that met the following criteria: FPKM > 1 and a fold change compared with the control of > 1.5 or < 0.67. The upstream cytokines predicted by IPA, along with their P-values and Z-scores, are shown in Fig. 4b.

Single cell isolation

Synovial tissues were collected from both knees of 10 control mice (20 knees) and 10 MMS D14 mice (20 knees), respectively, pooled within each group, and processed as a single sample for analysis. These tissues were minced with scissors, and transferred into RPMI-1640 (Nacalai Tesque) containing 0.2 mg/ml Liberase TL (Sigma-Aldrich) and 0.1 mg/ml DNase I (Roche) at 37℃ for 20 min, with intermittent syringe homogenization. Cells were filtered through 100- and 40-μm cell strainers, and a 40-μm Flowmi cell strainer (Sigma-Aldrich).

Generation of droplet-based scRNA-seq data

For each synovium sample, single-cell RNA libraries were generated using the 10x Genomics Chromium platform. Single-cell suspensions

were loaded onto the Chromium Single Cell System, v3.1 (Chromium Next GEM Single Cell 3′ Reagent Kit v3.1). Cells were diluted to a concentration of 1,000–1,500 cells/μl. Approximately 16,000 cells per sample were loaded into the Chromium chip, according to the Cell Suspension Volume Calculator Table, to capture transcripts from approximately 10,000 cells. We performed 13 cycles of cDNA amplification. The quality and quantity of the libraries were verified using a High-Sensitivity DNA Kit (Agilent Technologies) on a 2100 Bioanalyzer (Agilent Technologies). The libraries were sequenced on the NovaSeq 6000 platform (Illumina).

scRNA-seq *in silico* analysis

The protocol was summarized in our previous paper[58]. Fastq files were mapped onto the GENCODE mm39 primary assembly genome reference using STARsolo[59]. Cells were filtered with the following cutoff values (>1,000 genes/cell, %mt genes <10) and resulted in the following numbers of cells (5,677 control and 3,186 MMS cells, shown in Fig. 5 and 6. The data were integrated using scanpy[60] and scvi-tools[61] on Python, considering the batch effect including cell cycle, %mt, %ribo, and sampling timing. GO analysis was conducted using decoupler[62] with reference to the mSigDB database (m5.all.v2023.2.Mm.symbols.gmt). For the scRNA-seq analyses, differential gene expression was assessed in a pairwise manner within predefined comparisons.

Different genome assemblies were used for bulk RNA-seq (mm10) and scRNA-seq (mm39) analyses, reflecting the reference standards employed at the time of data generation and analysis. As downstream analyses were performed at the gene symbol level, this difference does not affect biological interpretation.

CLN injection

Intra-articular injections of 5 µl of CLNs (Hygieia Bioscience) were performed to deplete macrophages. Under anesthesia with isoflurane, CLNs were administered percutaneously using a Hamilton syringe with a 30 G needle. The initial injection was performed immediately prior to the initiation of tail suspension, and subsequent injections were administered every two weeks thereafter. Control liposomes were administered to control mice.

Statistical analyses

Statistical analyses were performed as described in each figure legend, using BellCurve for Excel ver. 3.20 (SSRI). Specifically, comparisons of two group means were analyzed using the two-tailed Mann–Whitney U test. For multiple comparisons, the Kruskal–Wallis test followed by the Steel–Dwass test was used. $P < 0.05$ was considered statistically significant for all tests. Bar charts in the data are presented as means ± standard deviation.

Data availability

The bulk and scRNA-seq data are available in the Gene Expression Omnibus under accession codes GSE200283 and GSE200898, respectively.

Ethics declarations

All mouse experiments were authorized to be approved by the Animal Care and Use Committee of the University of Tokyo (approval number M-P17-091). All methods were carried out in accordance with the relevant guidelines and regulations. All methods are reported in accordance with the ARRIVE guidelines (https://arriveguidelines.org).

Author contributions

HI and TS designed the research project. HI, YK, JH, JM, NT, and KN performed histological experiments. HI, and RC performed RNA-seq and scRNA-seq on the advice of MS and YS. HI and HO conducted bioinformatics analysis. HI, AT, FY, YO, and TS performed figure editing. HI and TS wrote the manuscript with critical input from HO, YS, RB, and ST.

Acknowledgments

We thank Junko Sugita, Keiko Kaneko, and Ryoko Honma for their technical assistance. We also extend our gratitude to Dr. Mitsutaka

Yakabe (Geriatric Medicine, University of Tokyo) for teaching us the method for the mouse tail suspension model. We also thank Kazumi Abe and Yuuta Kuze (Laboratory of Systems Genomics, Department of Computational Biology and Medical Sciences, University of Tokyo) for their technical advice on scRNA-seq.

Funding

This work was supported by JSPS KAKENHI grants 23H05484, 23K27718, 23K27717, 21K19552, 20H03799, 19H05654, 19H05565, and 18KK0254; the Nakatomi Foundation; and grants from the Japan Orthopaedics and Traumatology Research Foundation and the Hip Joint Foundation of Japan.

Competing interests

The authors declare no competing interests.

References

1 Baker, K. *et al.* Relation of synovitis to knee pain using contrast-enhanced MRIs. *Ann Rheum Dis* **69**, 1779-1783, https://doi.org/10.1136/ard.2009.121426 (2010).

2 Felson, D. T. *et al.* Synovitis and the risk of knee osteoarthritis: the MOST Study. *Osteoarthritis Cartilage* **24**, 458-464, https://doi.org/10.1016/j.joca.2015.09.013 (2016).

3 Allen, K. D., Thoma, L. M. & Golightly, Y. M. Epidemiology of osteoarthritis. *Osteoarthritis Cartilage* **30**, 184-195, https://doi.org/10.1016/j.joca.2021.04.020 (2022).

4 O'Neill, T. W., McCabe, P. S. & McBeth, J. Update on the epidemiology, risk factors and disease outcomes of osteoarthritis. *Best Pract Res Clin Rheumatol* **32**, 312-326, https://doi.org/10.1016/j.berh.2018.10.007 (2018).

5 Chang, S. H. *et al.* Excessive mechanical loading promotes osteoarthritis through the gremlin-1-NF-kappaB pathway. *Nat Commun* **10**, 1442, https://doi.org/10.1038/s41467-019-09491-5 (2019).

6 Hinterwimmer, S. *et al.* Cartilage atrophy in the knees of patients after seven weeks of partial load bearing. *Arthritis Rheum* **50**, 2516-2520, https://doi.org/10.1002/art.20378 (2004).

7 Tunc, H. *et al.* Ultrasonographic measurement of the femoral cartilage thickness in hemiparetic patients after stroke. *Int J Rehabil Res* **35**, 203-207, https://doi.org/10.1097/MRR.0b013e3283532736 (2012).

8 Yilmaz, B., Demir, Y., Ozyoruk, E., Kesikburun, S. & Guzelkucuk, U. The effect of knee joint loading and immobilization on the femoral cartilage thickness in paraplegics. *Spinal Cord* **54**, 283-286, https://doi.org/10.1038/sc.2015.151 (2016).

9 Rolvien, T. & Amling, M. Disuse Osteoporosis: Clinical and Mechanistic Insights. *Calcif Tissue Int* **110**, 592-604, https://doi.org/10.1007/s00223-021-00836-1 (2022).

10 Chen, H. *et al.* The effects of a home-based exercise intervention on elderly patients with knee osteoarthritis: a quasi-experimental study. *BMC Musculoskelet Disord* **20**, 160, https://doi.org/10.1186/s12891-019-2521-4 (2019).

11 de Matos Brunelli Braghin, R. *et al.* The effect of low-level laser therapy and physical exercise on pain, stiffness, function, and spatiotemporal gait variables in subjects with bilateral knee osteoarthritis: a blind randomized

clinical trial. *Disabil Rehabil* **41**, 3165-3172, https://doi.org/10.1080/09638288.2018.1493160 (2019).

12 Ojoawo, A. O., Olaogun, M. O. & Hassan, M. A. Comparative effects of proprioceptive and isometric exercises on pain intensity and difficulty in patients with knee osteoarthritis: A randomised control study. *Technol Health Care* **24**, 853-863, https://doi.org/10.3233/THC-161234 (2016).

13 Buechler, M. B. *et al.* Cross-tissue organization of the fibroblast lineage. *Nature* **593**, 575-579, https://doi.org/10.1038/s41586-021-03549-5 (2021).

14 Culemann, S. *et al.* Locally renewing resident synovial macrophages provide a protective barrier for the joint. *Nature* **572**, 670-675, https://doi.org/10.1038/s41586-019-1471-1 (2019).

15 Cochain, C. *et al.* Single-Cell RNA-Seq Reveals the Transcriptional Landscape and Heterogeneity of Aortic Macrophages in Murine Atherosclerosis. *Circ Res* **122**, 1661-1674, https://doi.org/10.1161/CIRCRESAHA.117.312509 (2018).

16 Martin, J. C. *et al.* Single-Cell Analysis of Crohn's Disease Lesions Identifies a Pathogenic Cellular Module Associated with Resistance to Anti-TNF Therapy. *Cell* **178**, 1493-1508 e1420, https://doi.org/10.1016/j.cell.2019.08.008 (2019).

17 Alivernini, S. *et al.* Distinct synovial tissue macrophage subsets regulate inflammation and remission in rheumatoid arthritis. *Nat Med* **26**, 1295-1306, https://doi.org/10.1038/s41591-020-0939-8 (2020).

18 Chou, C. H. *et al.* Synovial cell cross-talk with cartilage plays a major role in the pathogenesis of osteoarthritis. *Sci Rep* **10**, 10868, https://doi.org/10.1038/s41598-020-67730-y (2020).

19 Zhang, F. *et al.* Defining inflammatory cell states in rheumatoid arthritis joint synovial tissues by integrating single-cell transcriptomics and mass cytometry. *Nat Immunol* **20**, 928-942, https://doi.org/10.1038/s41590-019-0378-1 (2019).

20 Li, H. *et al.* Levels of metalloproteinase (MMP-3, MMP-9), NF-kappaB ligand (RANKL), and nitric oxide (NO) in peripheral blood of osteoarthritis (OA) patients. *Clin Lab* **58**, 755-762 (2012).

21 Zeng, G. Q., Chen, A. B., Li, W., Song, J. H. & Gao, C. Y. High MMP-1, MMP-2, and MMP-9 protein levels in osteoarthritis. *Genet Mol Res* **14**, 14811-14822 (2015).

22 Li, S. *et al.* COL3A1 and MMP9 Serve as Potential Diagnostic Biomarkers of

Osteoarthritis and Are Associated With Immune Cell Infiltration. *Front Genet* **12**, 721258, https://doi.org/10.3389/fgene.2021.721258 (2021).

23 Rhee, J. W. *et al.* Regulation of matrix metalloproteinase-9 gene expression and cell migration by NF-kappa B in response to CpG-oligodeoxynucleotides in RAW 264.7 cells. *Mol Immunol* **44**, 1393-1400, https://doi.org/10.1016/j.molimm.2006.05.003 (2007).

24 Saito, T. & Tanaka, S. Molecular mechanisms underlying osteoarthritis development: Notch and NF-kappaB. *Arthritis Res Ther* **19**, 94, https://doi.org/10.1186/s13075-017-1296-y (2017).

25 Yu, Q. & Stamenkovic, I. Cell surface-localized matrix metalloproteinase-9 proteolytically activates TGF-beta and promotes tumor invasion and angiogenesis. *Genes Dev* **14**, 163-176 (2000).

26 Frangogiannis, N. Transforming growth factor-β in tissue fibrosis. *J Exp Med* **217**, e20190103, https://doi.org/10.1084/jem.20190103 (2020)..

27 Dayer, C. & Stamenkovic, I. Recruitment of Matrix Metalloproteinase-9 (MMP-9) to the Fibroblast Cell Surface by Lysyl Hydroxylase 3 (LH3) Triggers Transforming Growth Factor-beta (TGF-beta) Activation and Fibroblast Differentiation. *J Biol Chem* **290**, 13763-13778, https://doi.org/10.1074/jbc.M114.622274 (2015).

28 Xu, D., Mu, R. & Wei, X. The Roles of IL-1 Family Cytokines in the Pathogenesis of Systemic Sclerosis. *Front Immunol* **10**, 2025, https://doi.org/10.3389/fimmu.2019.02025 (2019).

29 Meli VS, *et al.* YAP-mediated mechanotransduction tunes the macrophage inflammatory response. *Sci Adv* **6**, https://doi.org/10.1126/sciadv.abb8471. (2020)

30 Lee M, Du H, Winer DA, Clemente-Casares X, Tsai S. Mechanosensing in macrophages and dendritic cells in steady-state and disease. *Front Cell Dev Biol* **10**, 1044729, https://doi.org/10.3389/fcell.2022.1044729 (2022).

31 Gilbert, S. J., Bonnet, C. S. & Blain, E. J. Mechanical Cues: Bidirectional Reciprocity in the Extracellular Matrix Drives Mechano-Signalling in Articular Cartilage. *Int J Mol Sci* **22**, https://doi.org/10.3390/ijms222413595 (2021).

32 Rhee, D. K. *et al.* The secreted glycoprotein lubricin protects cartilage surfaces and inhibits synovial cell overgrowth. *J Clin Invest* **115**, 622-631, https://doi.org/10.1172/JCI22263 (2005).

33 Peters, B. *et al.* Protein-losing enteropathy in camptodactyly-arthropathy-

coxa vara-pericarditis (CACP) syndrome. *Pediatr Rheumatol Online J* **14**, 32, https://doi.org/10.1186/s12969-016-0093-5 (2016).

34 Ogawa, H., Kozhemyakina, E., Hung, H. H., Grodzinsky, A. J. & Lassar, A. B. Mechanical motion promotes expression of Prg4 in articular cartilage via multiple CREB-dependent, fluid flow shear stress-induced signaling pathways. *Genes Dev* **28**, 127-139, https://doi.org/10.1101/gad.231969.113 (2014).

35 Maenohara, Y. *et al.* Lubricin Contributes to Homeostasis of Articular Cartilage by Modulating Differentiation of Superficial Zone Cells. *J Bone Miner Res* **36**, 792-802, https://doi.org/10.1002/jbmr.4226 (2021).

36 Croft, A. P. *et al.* Distinct fibroblast subsets drive inflammation and damage in arthritis. *Nature* **570**, 246-251, https://doi.org/10.1038/s41586-019-1263-7 (2019).

37 Mizoguchi, F. *et al.* Functionally distinct disease-associated fibroblast subsets in rheumatoid arthritis. *Nat Commun* **9**, 789, https://doi.org/10.1038/s41467-018-02892-y (2018).

38 Papadaki, M. *et al.* New Insights for RANKL as a Proinflammatory Modulator in Modeled Inflammatory Arthritis. *Front Immunol* **10**, 97, https://doi.org/10.3389/fimmu.2019.00097 (2019).

39 Bakker, A. C. *et al.* Overexpression of active TGF-beta-1 in the murine knee joint: evidence for synovial-layer-dependent chondro-osteophyte formation. *Osteoarthritis Cartilage* **9**, 128-136, https://doi.org/10.1053/joca.2000.0368 (2001).

40 Scharstuhl, A. *et al.* Inhibition of endogenous TGF-beta during experimental osteoarthritis prevents osteophyte formation and impairs cartilage repair. *J Immunol* **169**, 507-514, https://doi.org/10.4049/jimmunol.169.1.507 (2002).

41 Xie, L. *et al.* Systemic neutralization of TGF-beta attenuates osteoarthritis. *Ann N Y Acad Sci* **1376**, 53-64, https://doi.org/10.1111/nyas.13000 (2016).

42 Jiao, K. *et al.* Overexpressed TGF-beta in subchondral bone leads to mandibular condyle degradation. *J Dent Res* **93**, 140-147, https://doi.org/10.1177/0022034513513034 (2014).

43 Tsukui, T. *et al.* Qualitative rather than quantitative changes are hallmarks of fibroblasts in bleomycin-induced pulmonary fibrosis. *Am J Pathol* **183**, 758-773, https://doi.org/10.1016/j.ajpath.2013.06.005 (2013).

44 Kapoor, M., Martel-Pelletier, J., Lajeunesse, D., Pelletier, J. P. & Fahmi, H. Role of proinflammatory cytokines in the pathophysiology of osteoarthritis.

Nat Rev Rheumatol **7**, 33-42, https://doi.org/10.1038/nrrheum.2010.196 (2011).

45 Coryell, P. R., Diekman, B. O. & Loeser, R. F. Mechanisms and therapeutic implications of cellular senescence in osteoarthritis. *Nat Rev Rheumatol* **17**, 47-57, https://doi.org/10.1038/s41584-020-00533-7 (2021).

46 Khan, M. A. *et al.* Nonsurgically induced disuse muscle atrophy and neuromuscular dysfunction upregulates alpha7 acetylcholine receptors. *Can J Physiol Pharmacol* **92**, 1-8, https://doi.org/10.1139/cjpp-2013-0063 (2014).

47 Yokota, K. *et al.* Deterioration of bone microstructure by aging and menopause in Japanese healthy women: analysis by HR-pQCT. *J Bone Miner Metab* **38**, 826-838, https://doi.org/10.1007/s00774-020-01115-z (2020).

48 Cake, M. A. *et al.* Synovial pathology in an ovine model of osteoarthritis: effect of intraarticular hyaluronan (Hyalgan). *Clin Exp Rheumatol* **26**, 561-567 (2008).

49 van der Sluijs, J. A. *et al.* The reliability of the Mankin score for osteoarthritis. *J Orthop Res* **10**, 58-61, https://doi.org/10.1002/jor.1100100107 (1992).

50 Rajthala, S. *et al.* Combined In Situ Hybridization and Immunohistochemistry on Archival Tissues Reveals Stromal microRNA-204 as Prognostic Biomarker for Oral Squamous Cell Carcinoma. *Cancers (Basel)* **13**, https://doi.org/10.3390/cancers13061307 (2021).

51 Ge, S. X., Son, E. W. & Yao, R. iDEP: an integrated web application for differential expression and pathway analysis of RNA-Seq data. *BMC Bioinformatics* **19**, 534, https://doi.org/10.1186/s12859-018-2486-6 (2018).

52. R Core Team. R: A Language and Environment for Statistical Computing, Version 4.4.1. Vienna, Austria https://www.r-project.org/ (2024).

53 Wickham H. ggplot2: Elegant Graphics for Data Analysis (Springer New York, 2009).

54 Gu, Z. Complex heatmap visualization. *Imeta* **1**, e43, doi:10.1002/imt2.43 (2022).

55 Kuhn M, et al. corrr: Correlations in R https://github.com/tidymodels/corrr (2025).

56 Castanza, A. S. *et al.* Extending support for mouse data in the Molecular Signatures Database (MSigDB). *Nat Methods* **20**, 1619-1620, https://doi.org/10.1038/s41592-023-02014-7 (2023).

57 Kramer, A., Green, J., Pollard, J., Jr. & Tugendreich, S. Causal analysis approaches in Ingenuity Pathway Analysis. *Bioinformatics* **30**, 523-530, https://doi.org/10.1093/bioinformatics/btt703 (2014).

58 Okada, H., Chung, U. I. & Hojo, H. Correction: Practical Compass of Single-Cell RNA-Seq Analysis. *Curr Osteoporos Rep* **22**, 299, https://doi.org/10.1007/s11914-024-00861-7 (2024).

59 Kaminow B, et al. STARsolo: accurate, fast and versatile mapping/quantification of single-cell and single-nucleus RNA-seq data. Preprint at https://doi.org/10.1101/2021.05.05.442755 (2021).

60 Wolf, F. A., Angerer, P. & Theis, F. J. SCANPY: large-scale single-cell gene expression data analysis. *Genome Biol* **19**, 15, https://doi.org/10.1186/s13059-017-1382-0 (2018).

61 Gayoso, A. *et al.* A Python library for probabilistic analysis of single-cell omics data. *Nat Biotechnol* **40**, 163-166, https://doi.org/10.1038/s41587-021-01206-w (2022).

62 Badia, I. M. P. *et al.* decoupleR: ensemble of computational methods to infer biological activities from omics data. *Bioinform Adv* **2**, vbac016, https://doi.org/10.1093/bioadv/vbac016 (2022).

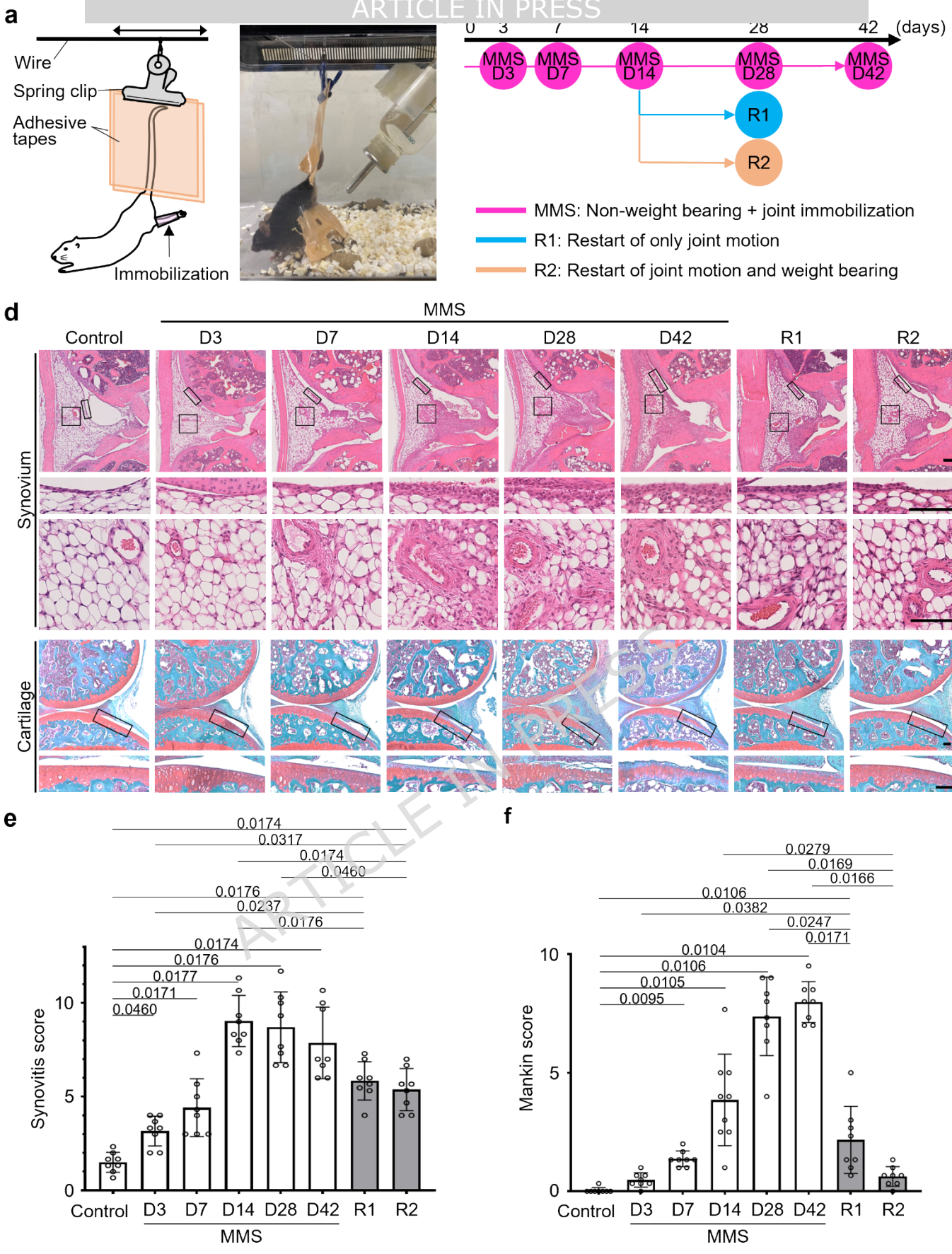

Fig. 1. Synovitis and cartilage degeneration induced by joint immobilization and unloading. (**a**) Schema of the minimized mechanical stress (MMS) model. Knee joints were immobilized by small plastic cylinders and kept in a non-weight-bearing condition by

tail suspension. (**b**) Actual setting of the MMS model. The mice could freely move around in the cage, eat, and drink. (**c**) Time course of the MMS model. The mice were evaluated at several time points. In addition to the standard MMS group, two groups were added: R1, where joint immobilization only was canceled at Day (D)14, while tail suspension was continued for an additional 14 days; R2, where both joint motion and weight bearing were allowed at D14. (**d**) Representative hematoxylin and eosin and safranin O staining of synovium and cartilage in the sagittal plane. Inset boxes in the upper panels indicate the location of the enlarged images below. Scale bars: 100 μm. (**e, f**) Synovitis score (**e**) and modified Mankin score (**f**) at each time point (n = 8 mice). Statistics: Kruskal–Wallis test followed by Steel–Dwass multiple comparison (**e, f**).

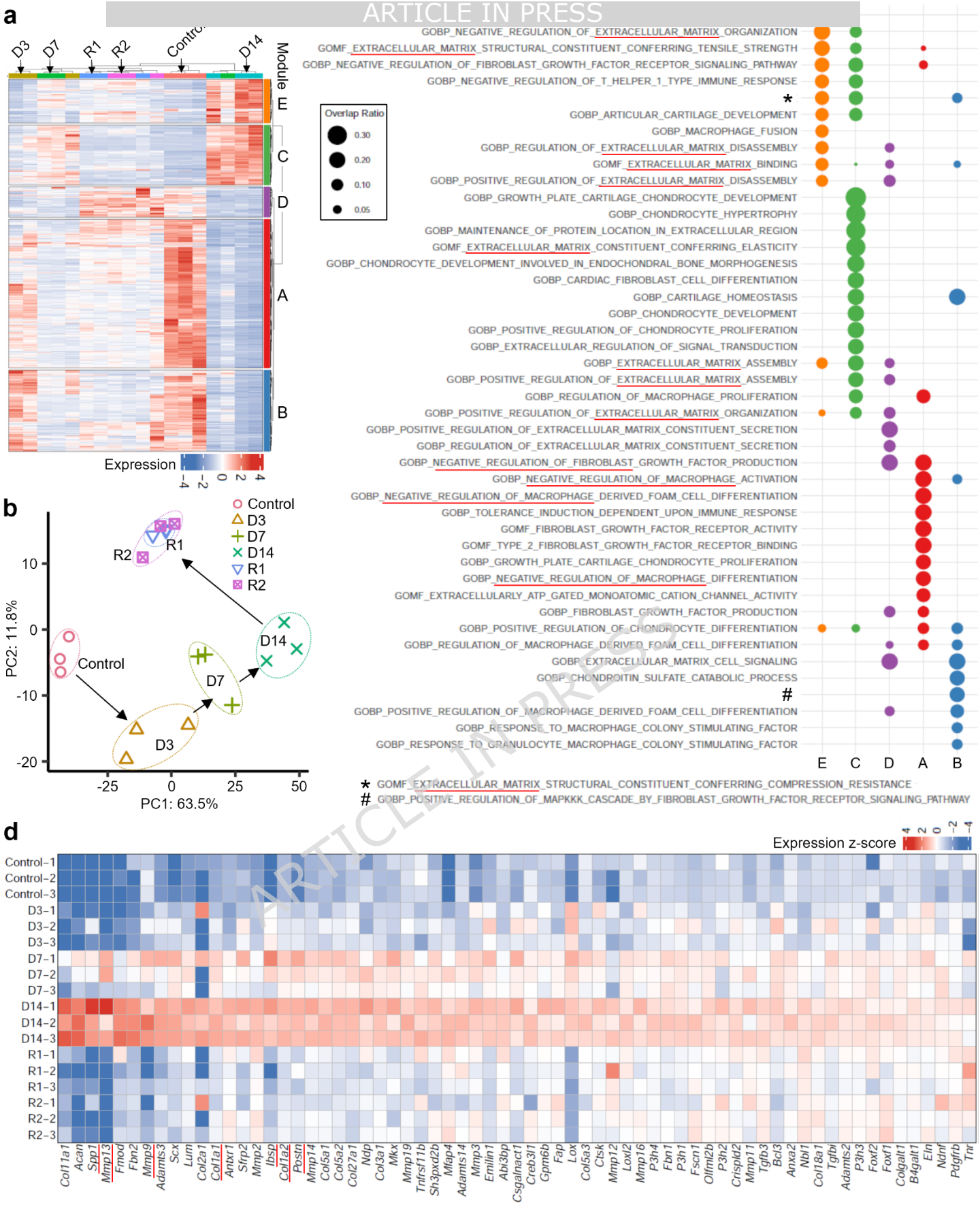

Fig. 2. Bulk RNA sequencing (RNA-seq) analyses of MMS synovium. (**a, b**) Heatmap (**a**) and principal component analysis (PCA) (**b**) of the top variable genes in each synovium sample (n = 3 mice). (**c**) Top 10 Gene Ontology (GO) terms enriched in five gene

modules. The analysis was performed based on genes related to terms including “fibroblast,” “extracellular,” “chondro,” “cartilage,” “inflammation,” “immune,” “macrophage,” or “mechano.” (**d**) Expression of representative genes related to GO terms including “extracellular matrix” or “collagen” in the synovium.

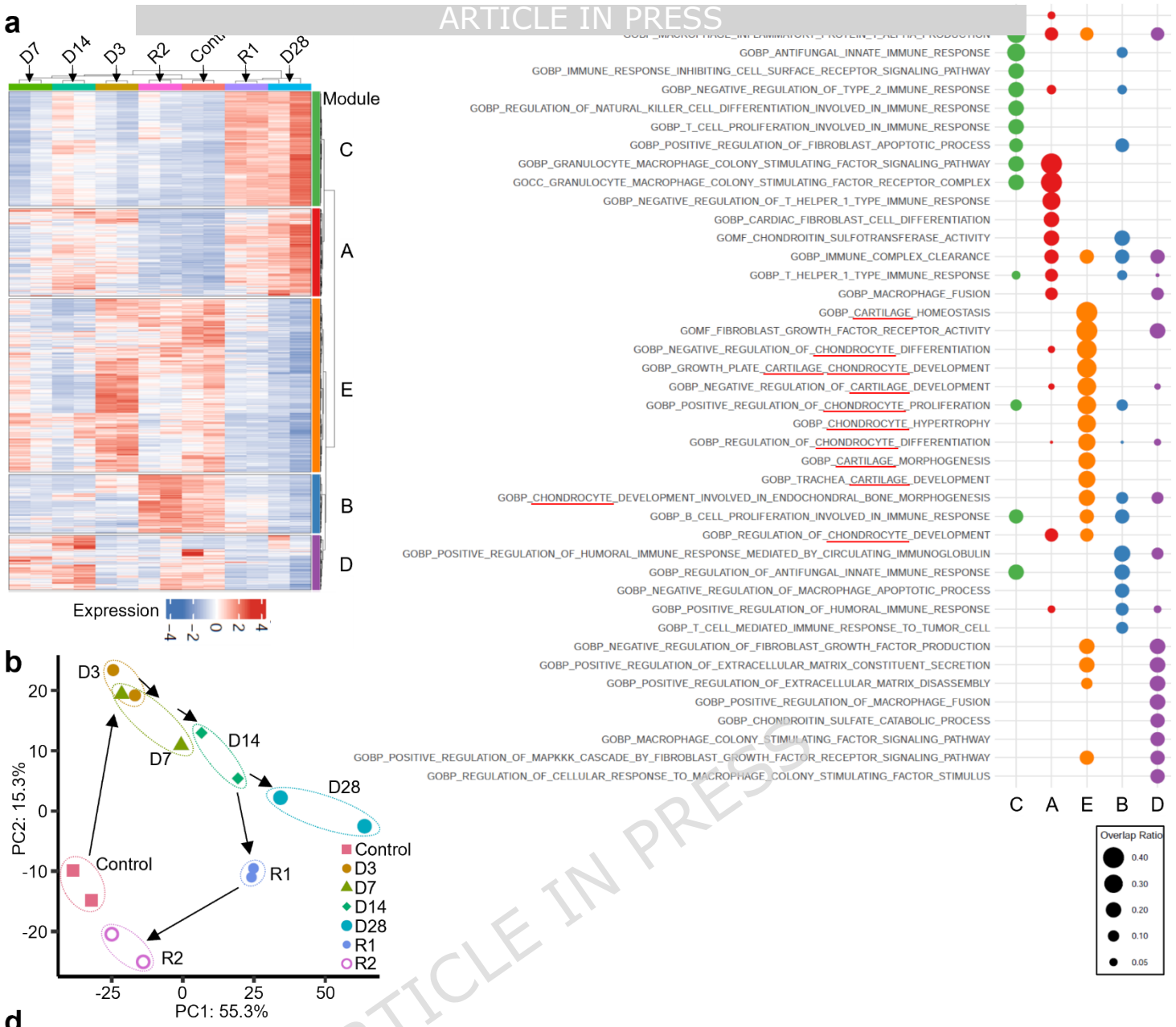

Fig. 3. Bulk RNA-seq analyses of MMS cartilage. (**a, b**) Heatmap (**a**) and PCA (**b**) of the variable genes in each cartilage sample (n = 2 mice). (**c**) Top 10 GO terms enriched in five gene modules. The analysis was performed based on genes related to terms including “fibroblast,” “extracellular,” “chondro,” “cartilage,” “inflammation,” “immune,” “macrophage,” or “mechano.”. (**d**) Expression of representative genes related to GO terms including “cartilage” or “tissue remodeling” in the cartilage.

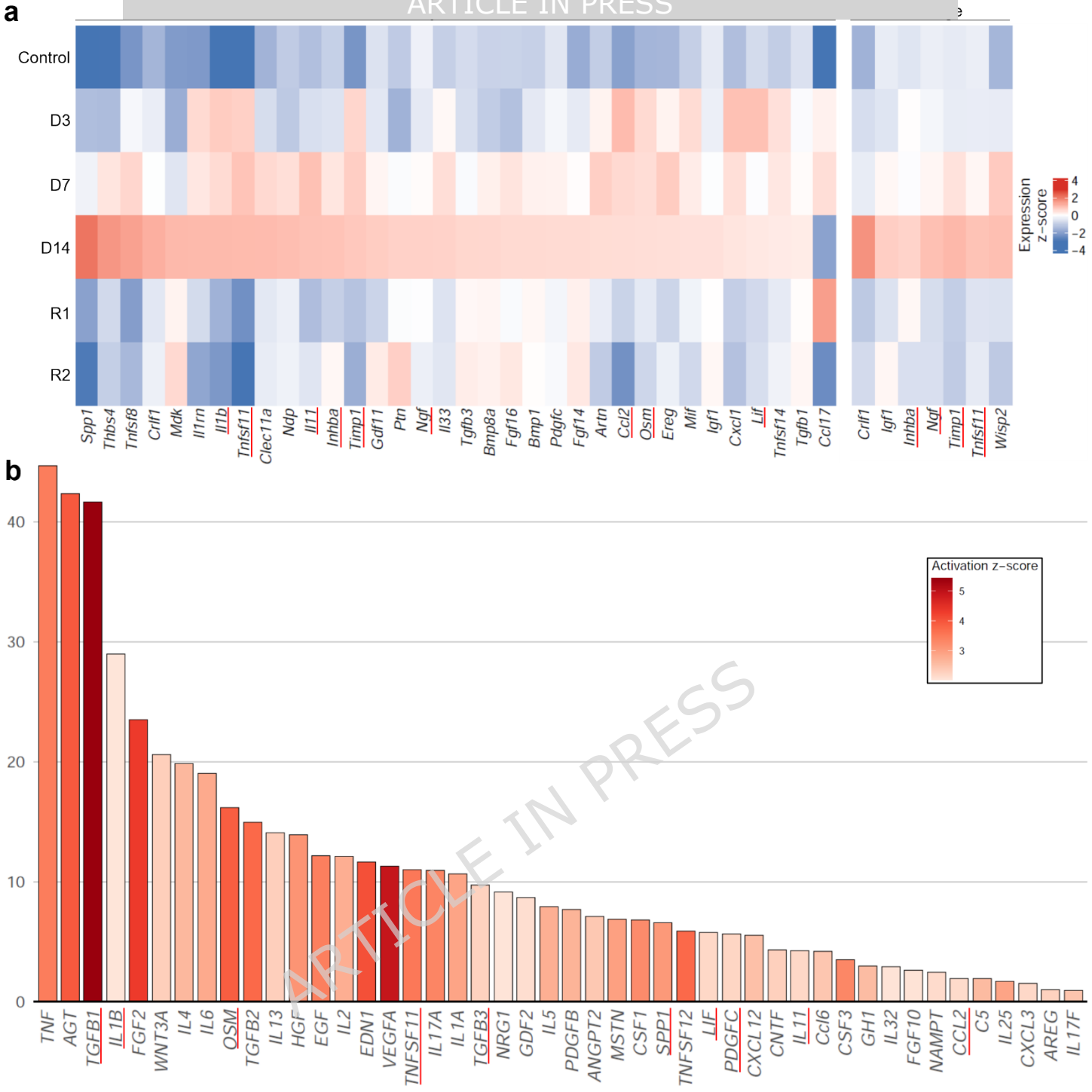

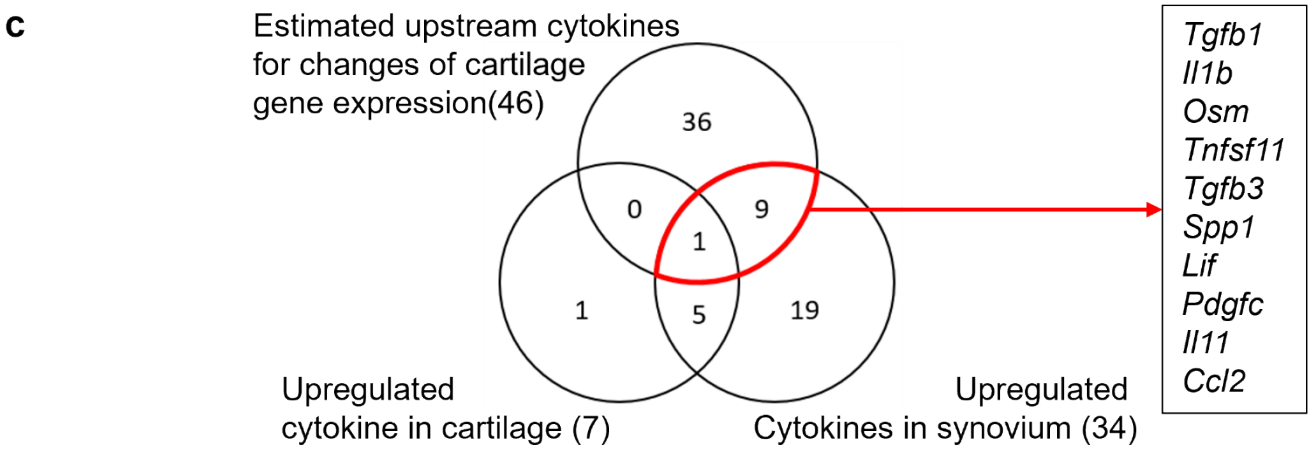

Fig. 4. MMS synovium expresses secreted proinflammatory cytokines, possible upstream regulators for cartilage degeneration. (a) Heatmap of representative cytokine expression that increased in MMS synovium and cartilage from the bulk RNA-seq data. (**b**) Candidate secreted molecules identified as upstream regulators of cartilage gene expression alterations by ingenuity pathway analysis (IPA) (**c**) Narrowing-down of candidates common between the results of the bulk RNA-seq and the IPA estimation.

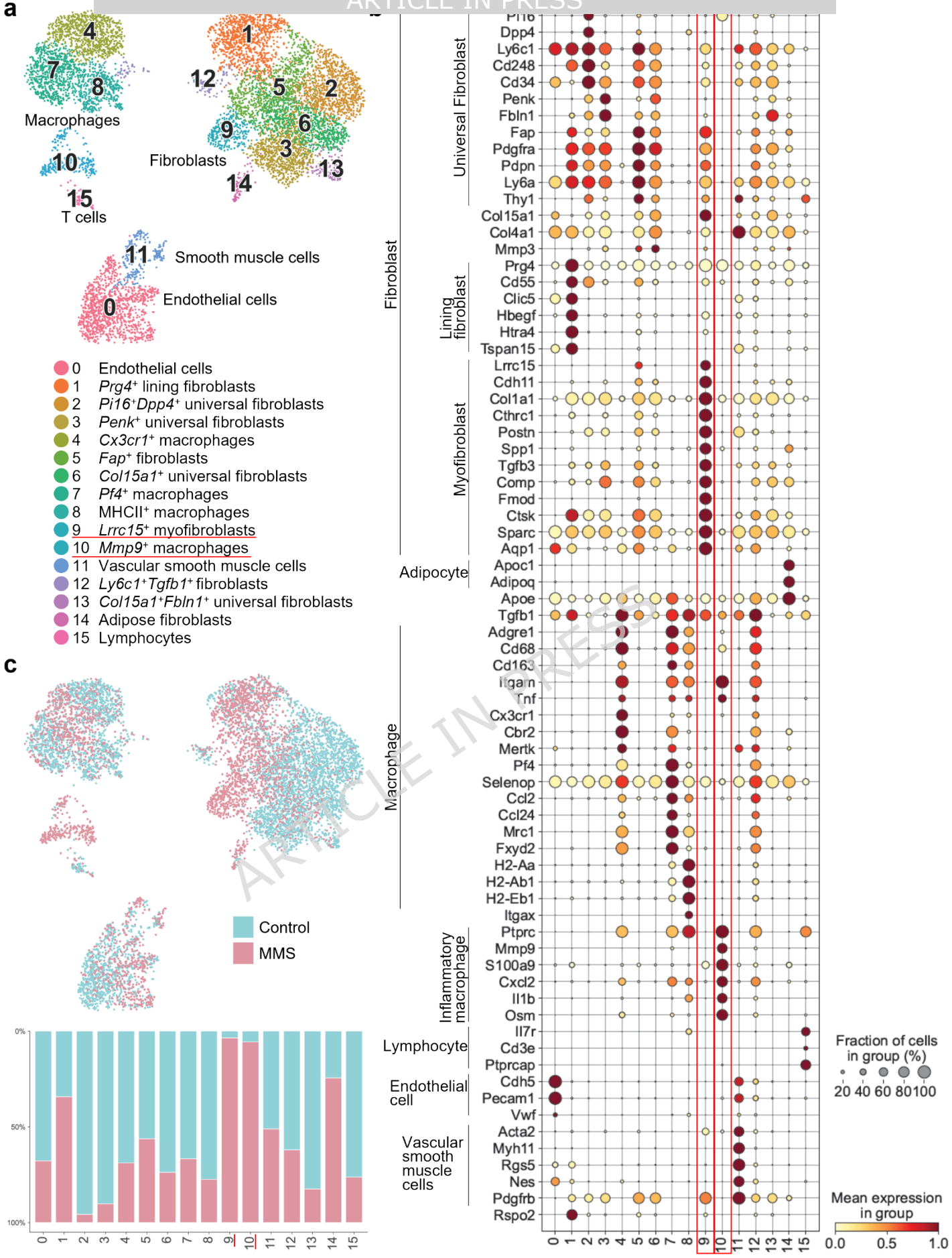

Fig. 5. Distinct fibroblast and macrophage subsets emerge in

MMS synovium. (**a**) Uniform manifold approximation and projection (UMAP) of synovial cells obtained from control and MMS mice, classified into 16 clusters. Synovial tissues were collected from both knees of 10 control mice (20 knees) and 10 MMS mice (20 knees). The mice were analyzed at D14. Twenty knees were used for each group. (**b**) Dot plot of marker genes for synovial fibroblasts and immune cells in the 16 clusters. (**c**) UMAP of synovial cells, indicating control or MMS groups. The graph below indicates the ratios of control and MMS in each cluster.

a Inflamma

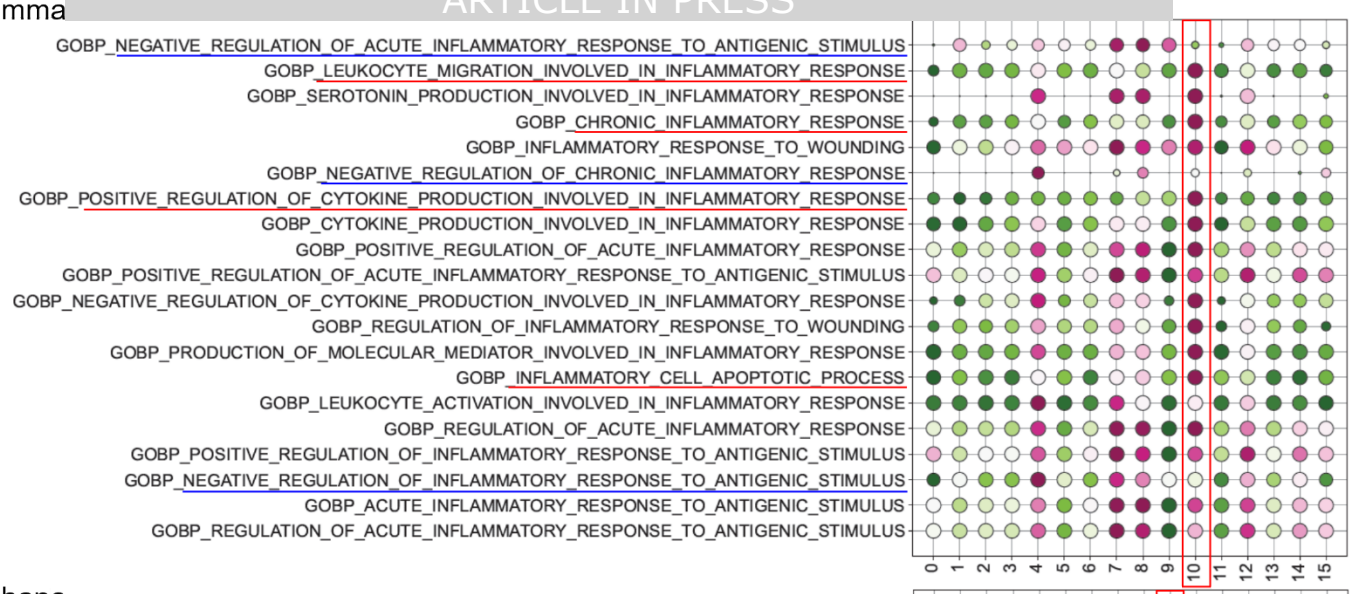

b Mechano

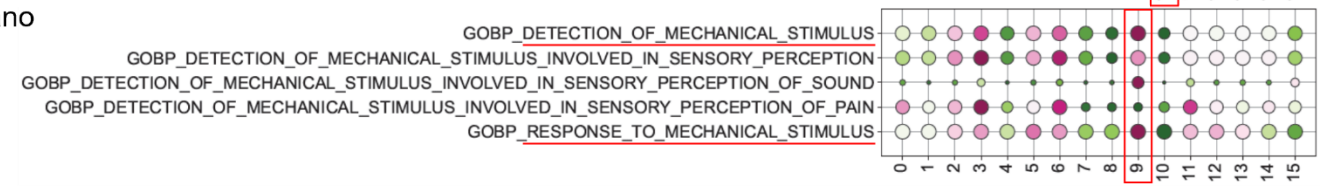

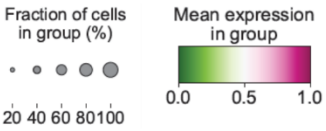

0	Endothelial cells	8	MHCII⁺ macrophages
1	*Prg4*⁺ lining fibroblasts	9	*Lrrc15*⁺ myofibroblasts
2	*Pi16*⁺*Dpp4*⁺ universal fibroblasts	10	*Mmp9*⁺ macrophages
3	*Penk*⁺ universal fibroblasts	11	Vascular smooth muscle cells
4	*Cx3cr1*⁺ macrophages	12	*Ly6c1*⁺*Tgfb1*⁺ fibroblasts
5	*Fap*⁺ fibroblasts	13	*Col15a1*⁺*Fbln1*⁺ universal fibroblasts
6	*Col15a1*⁺ universal fibroblasts	14	Adipose fibroblasts
7	*Pf4*⁺ macrophages	15	Lymphocytes

c

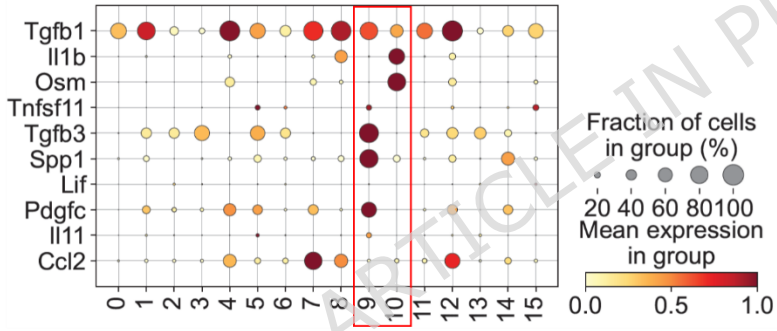

d

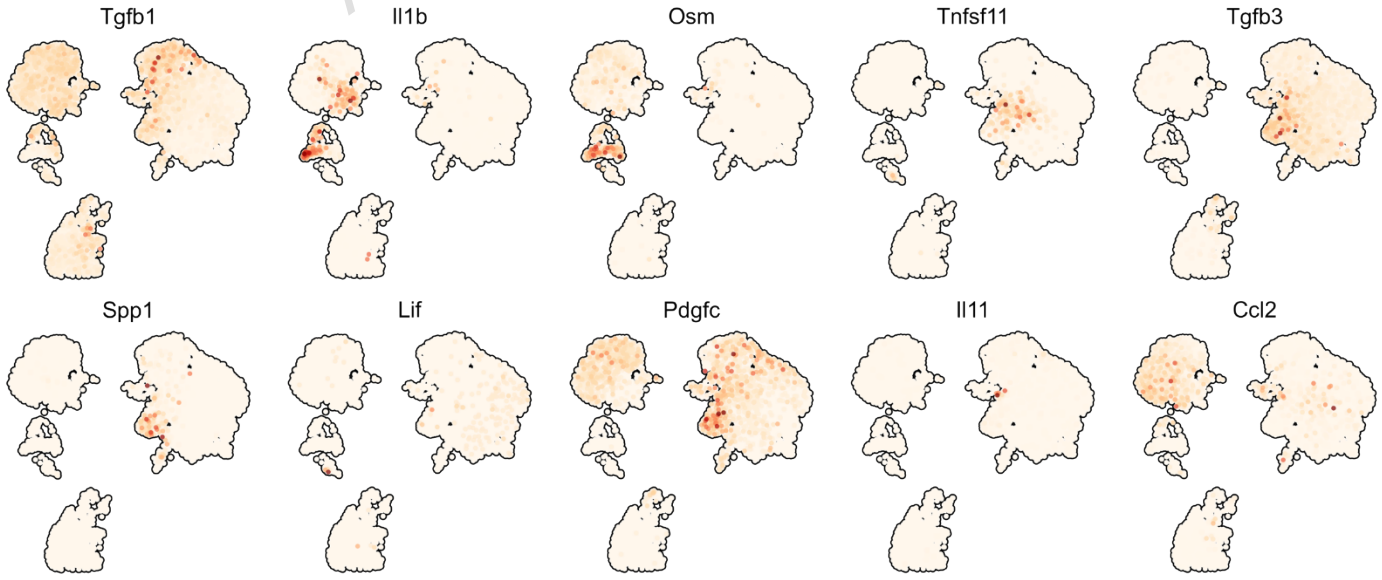

Fig. 6. Association of synovial cell clusters with MMS phenotypes. (**a, b**) Dot plots of representative GO terms related to “inflammatory” (**a**) and “mechano” (**b**) in the 16 clusters of control and MMS synovium. (**c, d**) Dot plot (**c**) and feature plots (**d**) of ten cytokine genes estimated as upstream regulators of MMS-induced cartilage changes (Fig. 4c).

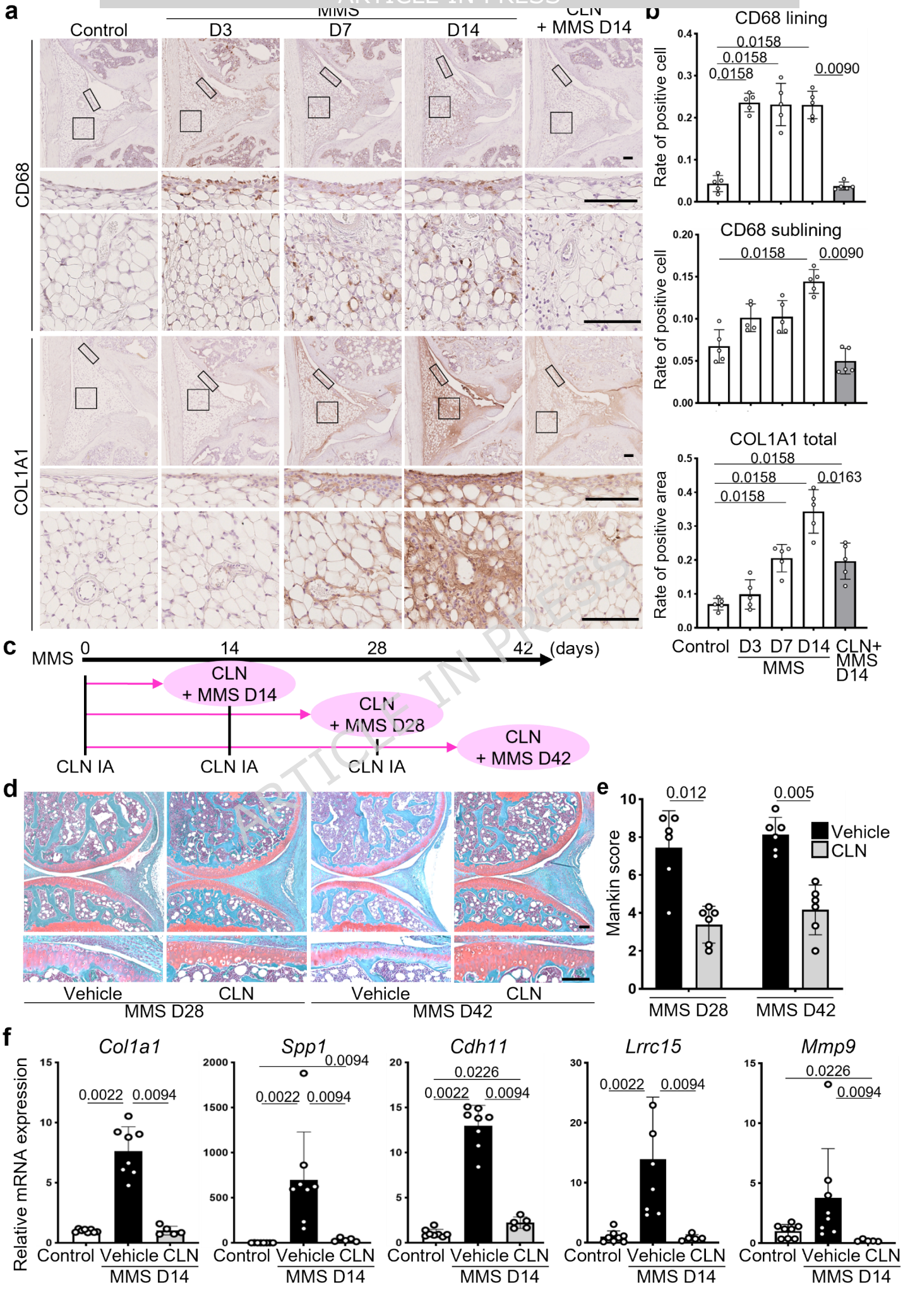

Fig. 7. Macrophages contribute to MMS phenotypes. (**a**) Representative immunohistochemistry of CD68 and COL1A1. Inset boxes in the upper panels indicate the location of the enlarged lining and sublining layer images in the lower panels. (**b**) Positive cell rates of CD68 in lining and sublining layers and the positive area of COL1A1. (**c**) Time course of clodronate liposome (CLN) injection. We intra-articularly administered 5 µl of CLN every 2 weeks. (**d, e**) Representative safranin O staining (**d**) and modified Mankin score (**e**) of cartilage in each group. Scale bars: 100 µm. (**f**) mRNA levels of marker genes for *Lrrc15*$^{+}$ fibroblasts and *Mmp9* in the synovium of each group: control, vehicle + MMS D14, and CLN + MMS D14. Statistics: Kruskal–Wallis test followed by Steel–Dwass multiple comparison (**b, f**). Two-tailed Mann–Whitney U test for comparison between MMS D14 and CLN + MMS D14 (**b**) and (**e**).

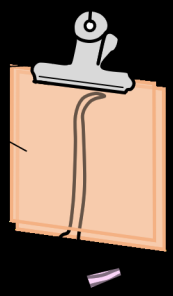

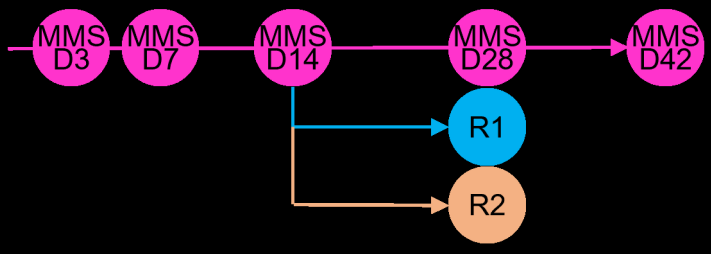
MMS D3
MMS D7
MMS D14
MMS D28
MMS D42
R1
R2

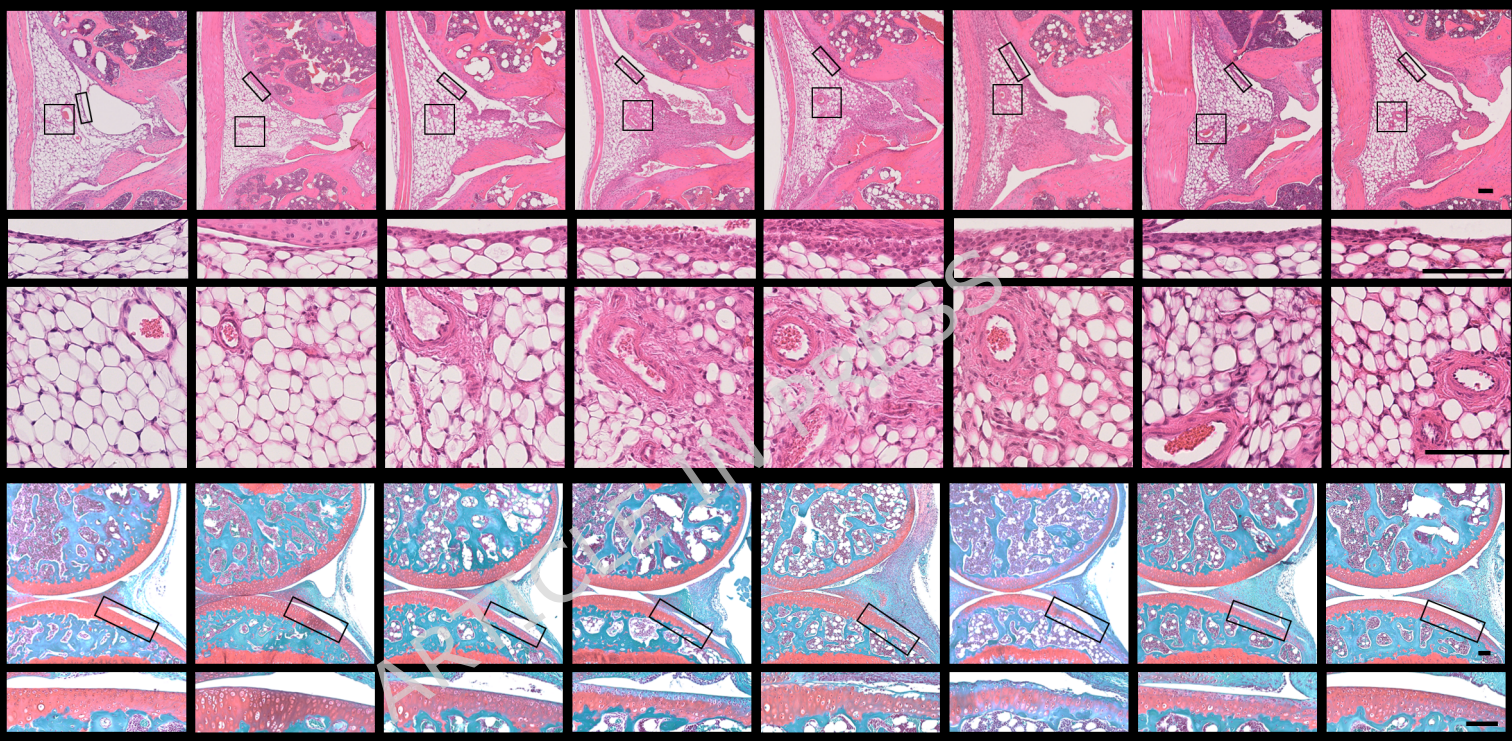

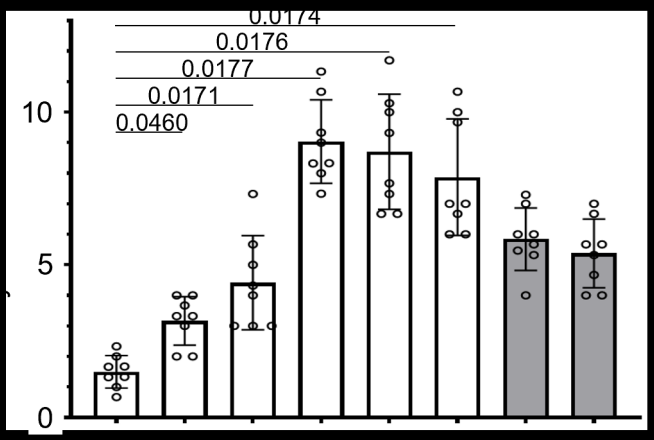
0.0174
0.0176
0.0177
0.0171
0.0460
10
5
0

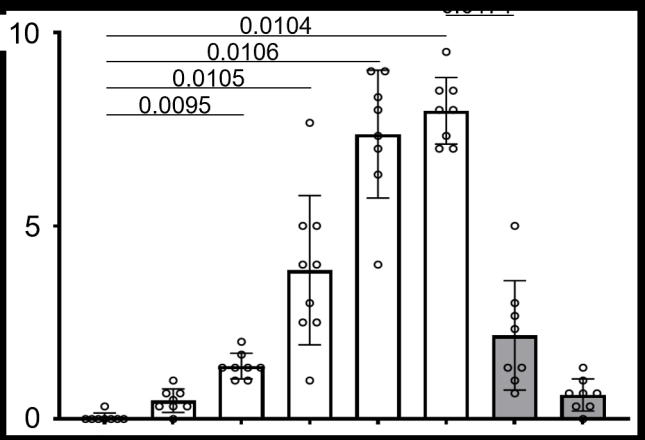
0.0104
0.0106
0.0105
0.0095
10
5
0

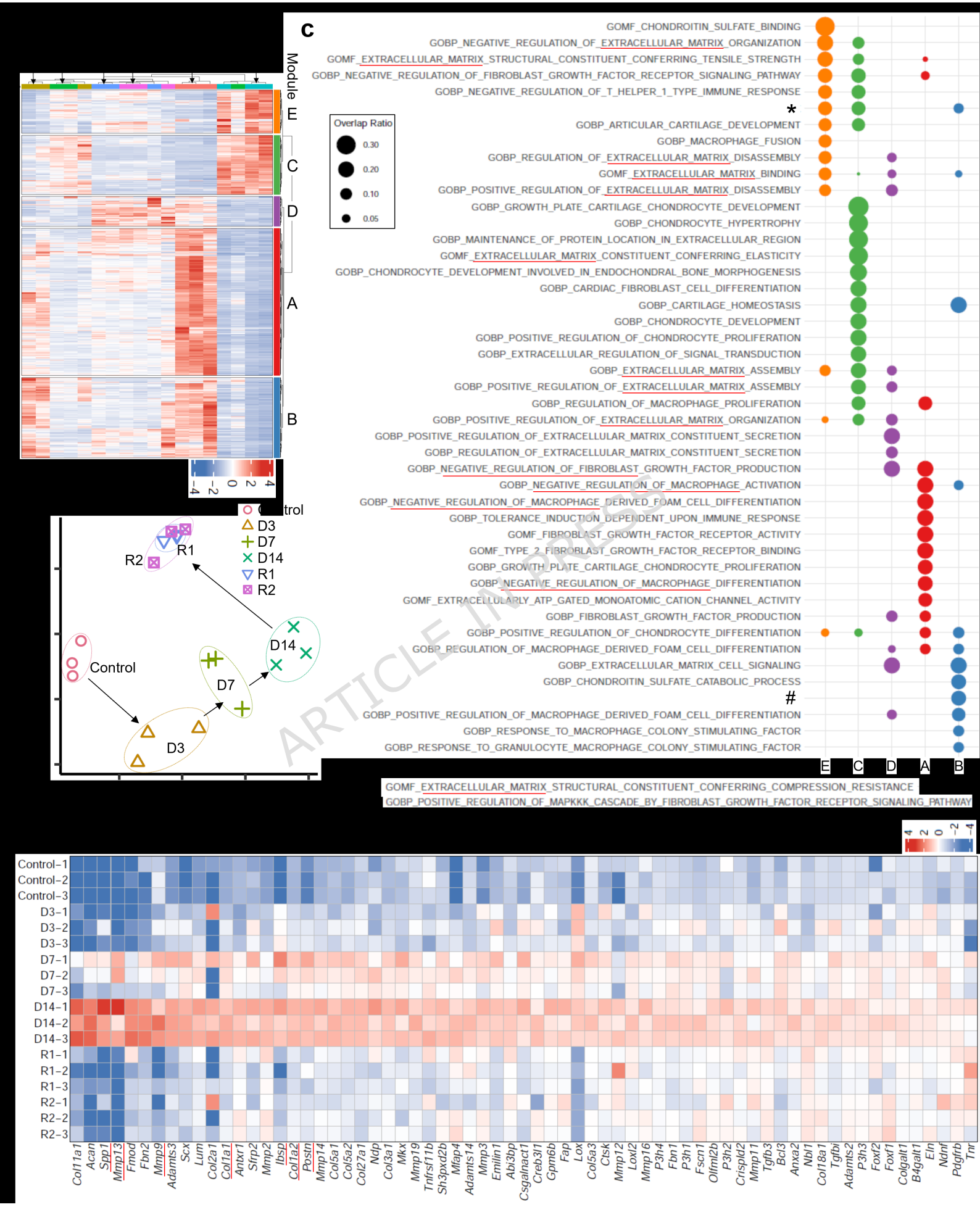

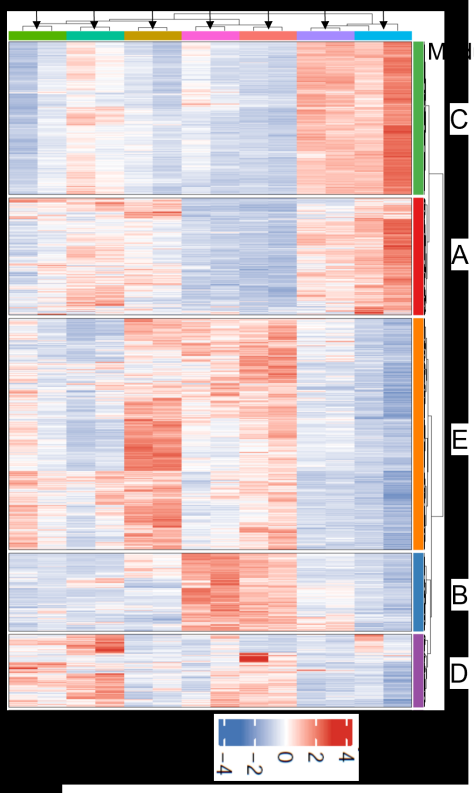

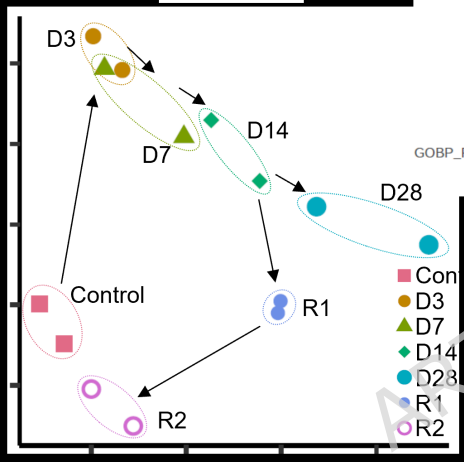

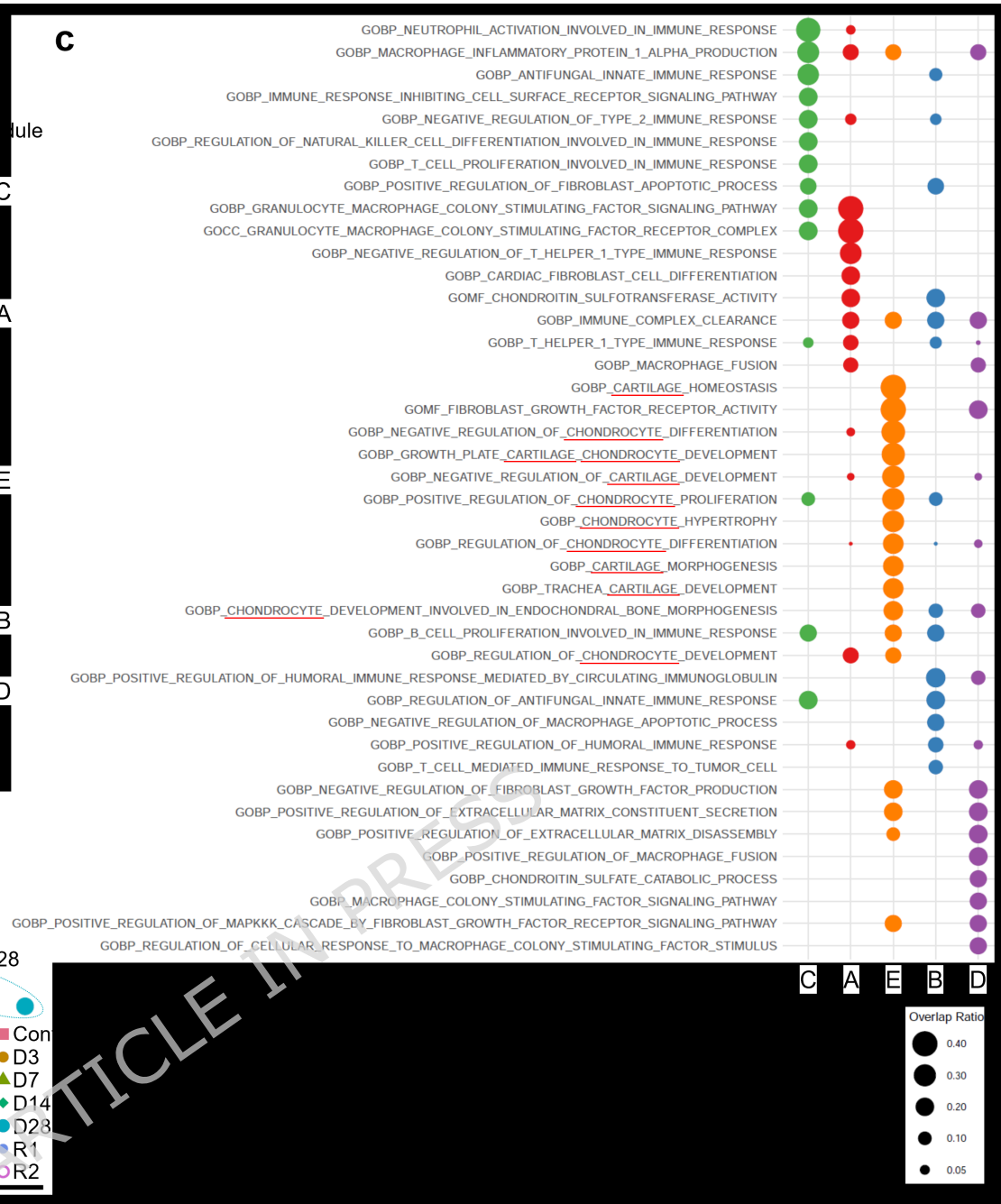

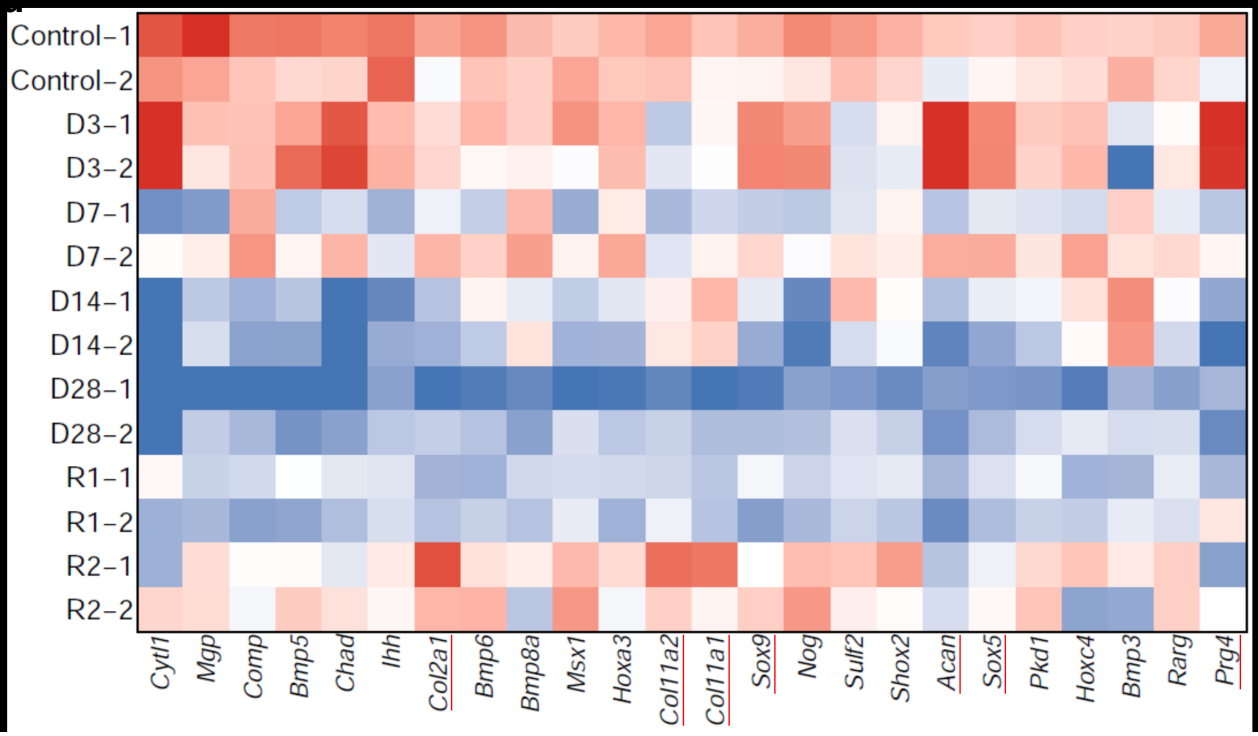

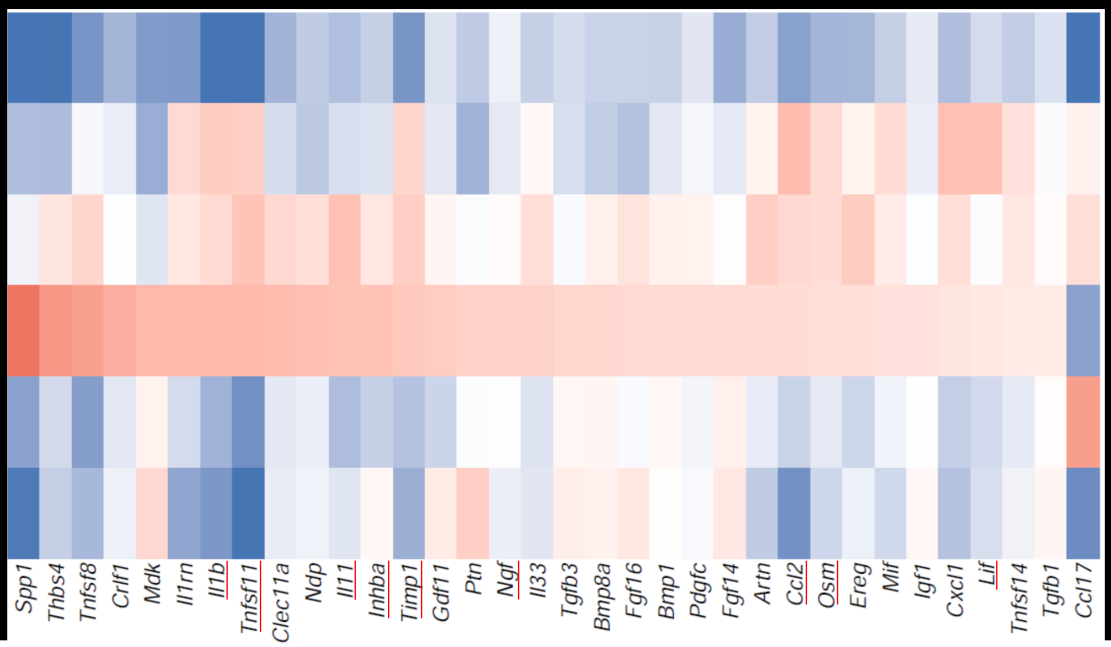

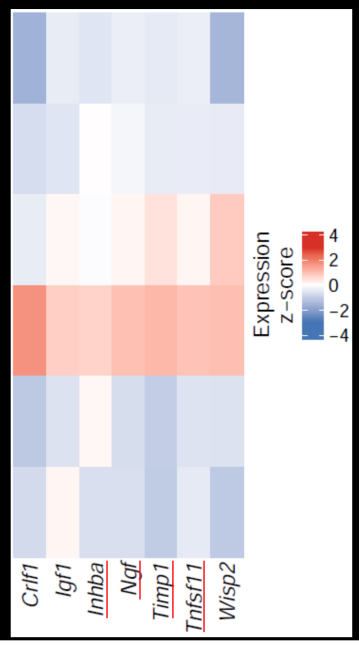

b